2008

# Spray deposition of biomolecular thin films

Mihir K. Rayan
*University of South Florida*

# Spray Deposition Of Biomolecular Thin Films

By

Mihir K Rayan

Submitted in partial fulfillment
of the requirements for the degree of
Masters of Science in Electrical Engineering
Department of Electrical Engineering
College of Engineering
University of South Florida

Major Professor: Rudy Schlaf, Ph.D
Andrew Hoff, Ph.D
Jing Wang, Ph.D

Date of Approval:
September 9, 2008

Keywords: airbrush, roughness, evanescent, immunoassay, residue

Dedication

To Dr. Schlaf for giving me the opportunity to work in the lab as an undergraduate and continue working as a graduate student.

Acknowledgements

I would like to thank Dr. Rudy Schlaf for his guidance, patience, and for giving me the opportunity for conducting research, Dr. Martin Beerbom for his experimental support, family and friends for their support. Additionally, I would like to thank the National Science Foundation and the College of Engineering REU program.

## Table Of Contents

## List Of Figures

## List Of Tables

## List Of Equations

Spray Deposition of Biomolecular Thin Films

Mihir K Rayan

## Abstract

In this paper, a parametric study of the airbrush deposition technique was investigated for the deposition biomolecular thin films. The airbrush parameters under investigation were intake valve opening, carrier gas pressure, distance between the airbrush and substrate, concentration of solution, vapor pressure of solvent, and hydrophobic/hydrophilic substrate surface. This study was assessed through the characterization of dried droplet residues of Bovine Serum Albumin (BSA) and of complete films of BSA by means of scanning electron microscopy (SEM) and atomic force microscopy (AFM). It was determined that droplet size was mainly affected by carrier gas pressure and vapor pressure. The parameters intake valve opening, distance between the airbrush and substrate, and concentration of solution control the rate of spray, or solution flux, onto the substrate. Solution flux was determined to have the greatest impact on film roughness. This allowed for flexibility in the airbrush deposition technique to produce films with various substrate wetting rates. Low flux films were produced when the droplets dried on the substrate surface before the next droplet arrived. High flux films were generated when droplets on the surface arrive before subsequent droplets are given time to dry. Finally, as an extension of the results of these experiments, a practical application of the airbrush deposition technique was conducted using appropriate deposition parameters. An E. coli wave guide biosensor was produced on a glass substrate. A sandwich immunoassay was used to confirm E. coli capture.

# Chapter 1

## Introduction

Organic thin films have found a host of applications in recent years in areas such as organic light emitting diodes [1], organic transistors [2], and organic solar cells [3, 4] . Deposition of organic materials is usually accomplished by solution processing [4]. Such techniques include ink-jet printing [5], spin coating [6] , sol-gel [7], screen-printing [8], and electrospray [9]. Deposition of biomolecules (i.e. naturally occurring organic molecules such as proteins) however has its own unique challenges. Biomolecules such as proteins are very large and complex. In general, protein molecules are sensitive to pH and temperature and may denature depending on environmental conditions [10]. Therefore, many conventional deposition methods are not suitable for deposition of functionally active proteins.

The airbrush deposition methodology is well suited for biomolecular deposition. Unlike electrospray for example, airbrush deposition does not require a conductive solution and substrate for deposition [11]. The airbrush method is simple and offers a continuous and fast deposition making it ideal for industrial application. Abner Peeler presented the first patent for an airbrush in 1882 [12]. Today, the modern handheld airbrush offers a high degree of atomization, permitting its use in many diverse

applications ranging from creating paintings [13], to cosmetic application [14], and to sunless tanning systems [15] among many others. Recently, the airbrush deposition has been employed in a variety of scientific applications as well [16-21].

This paper focuses on an exploration of the airbrush technique. While a number of examples for airbrush applications can be found in literature, particularly used spray parameters are only reported in rare instances. It appears that no systematic studies of the airbrush technique itself have been published to date. Four primary deposition parameters have been identified and chosen for investigation. The parameters are carrier gas pressure, intake valve opening, airbrush to substrate distance, and spray solution concentration. Additionally, the effect of the vapor pressure of the spray solution and the effect of the surface (hydrophobic verse hydrophilic) will be assessed on the average roughness of continuous films. The goal of this paper is to understand how the airbrush parameters affect film morphology, and to use this knowledge in the fabrication of an E. coli waveguide biosensor. The remainder of chapter 1 will be devoted to background information that is relevant to the experiments conducted in the subsequent chapters.

**Bovine Serum Albumin**

**Figure 1 - Serum Albumin**

Computer generated image of human serum albumin used as example of an albumin [22]

Serum Albumins in general are regulatory proteins and are generally used in transport mechanisms. Bovine Serum Albumin (BSA) was selected as a model biomolecule for deposition using the airbrush technique. BSA is one of the most extensively studied proteins [23] and is readily available. Figure 1 shown above, illustrates an image of the BSA molecule. The molecular weight of BSA has been cited as 66, 120 g/mol [24] and is composed of a single peptide chain containing no carbohydrates. Additionally, the protein dimensions were found to be 40 x 140 angstroms. In solution, BSA appears clear to slightly hazy and amber Figure 1 shows a three dimensional model of a serum albumin.

**Atomization**

The airbrush deposition technique involves spraying of liquid onto the substrate surface. A spray can be defined as "a dispersion of droplets with sufficient momentum to penetrate the surrounding medium [25]. Typically, the quality of a spray can be determined by its shape, its patternation, and some measure of droplet its droplet size[26]. In chapter 2, the effect of the droplet size of spray will be investigated as the airbrush parameters of carrier gas pressure, intake valve opening, airbrush to substrate distance, and concentration of spray solution is varied. The average droplet size will be indirectly determined by measuring the outer diameter of dried droplet BSA residues on a silicon substrate via scanning electron microscopy imaging.

**Figure 2 – Liquid jet breakup**

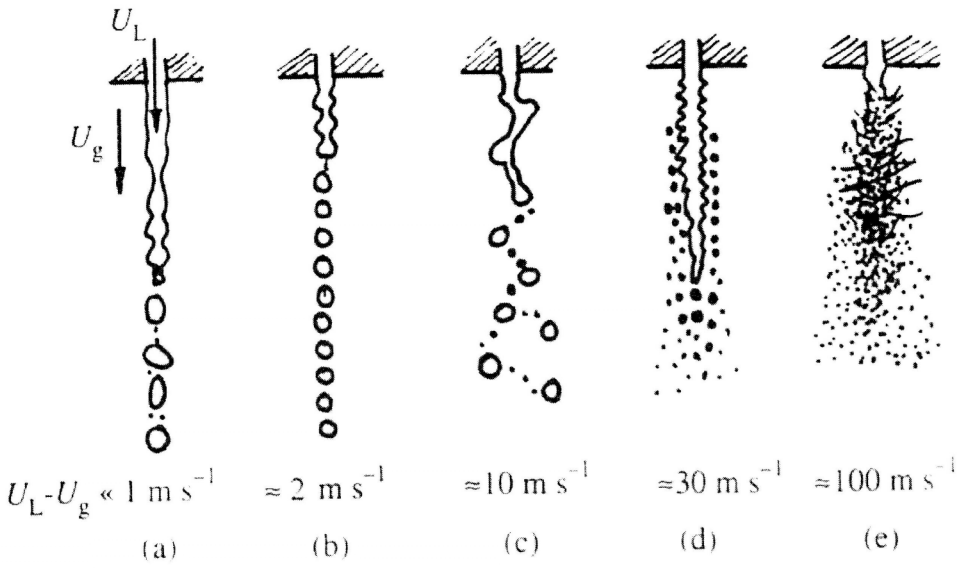


Illustration showing the behavior of liquid jet breakup. $U_L$ and $U_G$ represent the velocity of liquid and gas medium respectively [26]

There are believed to be two primary types of atomization termed primary atomization, occurring near the nozzle, and secondary atomization, occurring away from the nozzle [26]. The exact mechanism of atomization is still not fully understood, especially for very high flow rates, though many theories have been presented [27]. For example, Castleman proposed that atomization is due to the interaction between the liquid jet and surrounding gas medium [28]. Figure 2 shows the break up of a simple round liquid jet. $U_L$ and $U_G$ represent the velocity of the liquid and the surrounding gas, respectively. As the the difference between the liquid velocity and the surrounding gas velocity is increased, improved atomization and jet break up becomes evident.

In general, two numbers are used to describe the behavior of atomization termed the Weber number and the Reynolds number. In 1931 the effect of liquid viscosity on liquid jet atomization was investigated by Weber. The Weber number is a ratio of the inertia force to the surface tension force acting on the jet. The Reynolds number is a ratio of the inertial forces to the viscous forces. Increasing the Weber and Reynolds number tends to increase the rate and amount of atomization [26].

**Airbrush and general setup**

The airbrush used for the following experiments was obtained from Paasche (Paasche Airbrush Co. Chicago, USA) as part of a kit with the part number VL-SET and is a standard double action airbrush. The term *double action* refers to the ability to control the carrier gas output and solution output independently. Figure 3 illustrates the general experimental set for airbrush deposition. The rate of carrier gas output is controlled by the finger level assembly. Increased carrier gas output occurs as a result of depressing the finger level assembly. For all the experiments in this text, the finger-level assembly was fully depressed. The intake valve opening controls the amount of solution injection into the carrier gas stream and is controlled by an adjustable line screw (thumbwheel). Since the intake valve is hidden from view within the airbrush, the number of thumbwheel rotations was used to determine the intake valve setting. The airbrush and substrate were held apart by an adjustable threaded rod. Ultra high pure nitrogen was used as a carrier gas for deposition from a nitrogen gas cylinder. The carrier gas pressure was monitored at the regulator of the nitrogen gas cylinder.

**Figure 3 - General schematic setup**

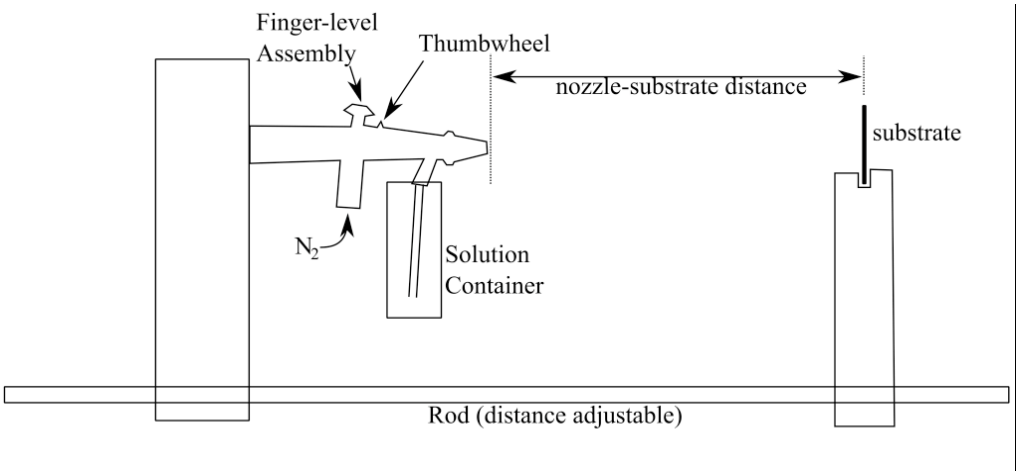


Schematic illustration showing the general setup for airbrush deposition.

## Vapor pressure

In chapter 3, the effect of the vapor pressure of the spray solution is investigated on the average roughness of films in both the high flux and low flux regimes. Three solvents were chosen in increasing vapor pressure. Vapor pressure is a measure of a substance's tendency to evaporate and is the force per unit area exerted by vapor in an equilibrium state with its surroundings at a given pressure and temperature[29]. The vapor pressure of a mixture can be considered the superposition of the vapor pressures of the individual solvents. The vapor pressures, at room temperature, of water, acetonitrile (ACN), and tetrahydrafuran (THF) are listed in table 1. Figure 4 shows the bond diagram of the solvents used in the spray solution.

**Table 1 - Vapor pressure of solvents at room temperature.**

| Solvent | Vapor pressure (torr) 25 C |
|---|---|
| Water | 18 |
| ACN | 89 |
| THF | 142 |

Table indicating the vapor pressure of solvents used in the spray solution at room temperature.

Water (figure 2a) is the most plentiful substance in living systems and makes up roughly 70 % of weight of organisms [30]. The water molecule is composed of an oxygen atom covalently bonded to two hydrogen atoms. Water is a polar solvent with a boiling point of 100 degrees Celsius. ACN (figure 2b) is a polar organic solvent composed of an ethyl group triple bonded to a nitrogen atom. ACN is colorless and miscible with water and has a boiling point of approximately 82 degrees Celsius. THF (figure 1c) is a cyclic, colorless, polar organic solvent that has a boiling point of approximately 66 degrees Celcius.

**Figure 4 – Bond diagram of solvents**

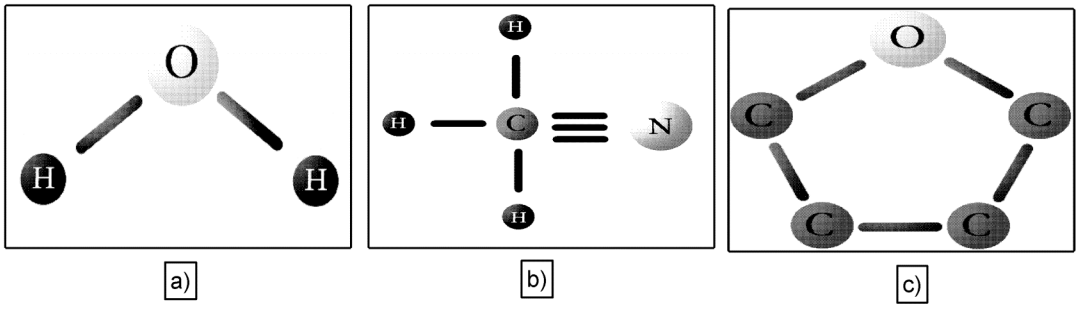


Figures illustrating bond diagram of (a) water, (b) acteonitrile, and (c) tetrahydofuran.

**Hydrophilic surface**

The effect of the surface on film quality has been studied for a number of deposition methods. In chapter 3, the effects of hydrophilic and hydrophobic surfaces on the average film roughness of complete films were investigated. A peroxide solution chemical oxidation was performed using the RCA SC- 1 method [31] as follows:

1. Create a mixture containing of DI water and (27 %) ammonium hydroxide (5:1)
2. Heat mixture until a temperature of 70 ± 5 degrees Celsius is achieved
3. Add (30 %) hydrogen peroxide to the mixture such that ratio becomes (5: 1: 1) DI water: ammonium hydroxide: hydrogen peroxide.
4. Immerse sample into solution for 15 minutes
5. Rinse with DI water.

The RCA SC-1 procedure is typically followed by a dilute HF etch to remove the newly formed thin oxide layer as a result of chemical oxidation. The formation of the clean oxide layer is known to be hydrophilic.

**Hydrophobic surface**

A hydrophobic surface was created by hydrogen passivation of silicon. A peroxide solution chemical oxidation (RCA SC-1 as described above) was performed to

ensure that any residual carbon contamination would be oxidized. Finally, the samples were subjected to dilute HF acid (10 %) for three minutes. The HF etching process removes the oxide layer and results in hydrogen passivation of the silicon. Figure 5 shows a schematic representation of the mechanism of hydrogen passivation. Hydrogen passivation begins with the fluorination of a free silicon bond on the surface by a fluorine ion. The silicon fluorine bond reconstructs the surface and makes the hydrogen- silicon bond more favorable than the silicon-silicon bond. With the addition more hydrogen fluoride, the bond passivation of the second layer of silicon continues [32]. Figure 5 d shows the final step of hydrogen passivation in the formation of silicon fluoride.

**Figure 5 - Hydrogen passivation [32]**

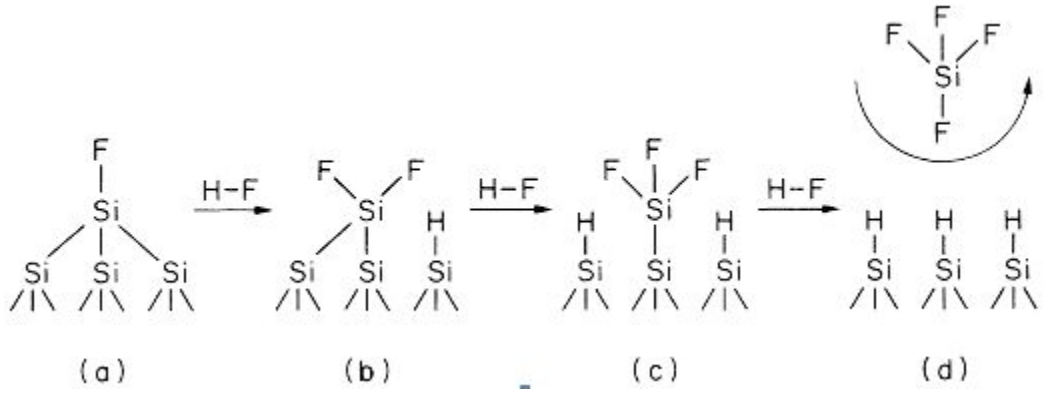


Process showing the hydrogen passiavtion of a silicon surface beginning with fluorination and ending with the creation of a silicon tetra fluoride molecule.

**Film quality**

There are many methods for accessing film quality. Examples include tensile strength measurement [33], conductivity measurement [34], and photoemission

spectroscopy[35, 36], among many others. In this text, the effect of the airbrush parameters on film quality is determined by scanning electron microscopy (SEM) and atomic force microscopy (AFM).

**Figure 6 – Scanning electron microscope**

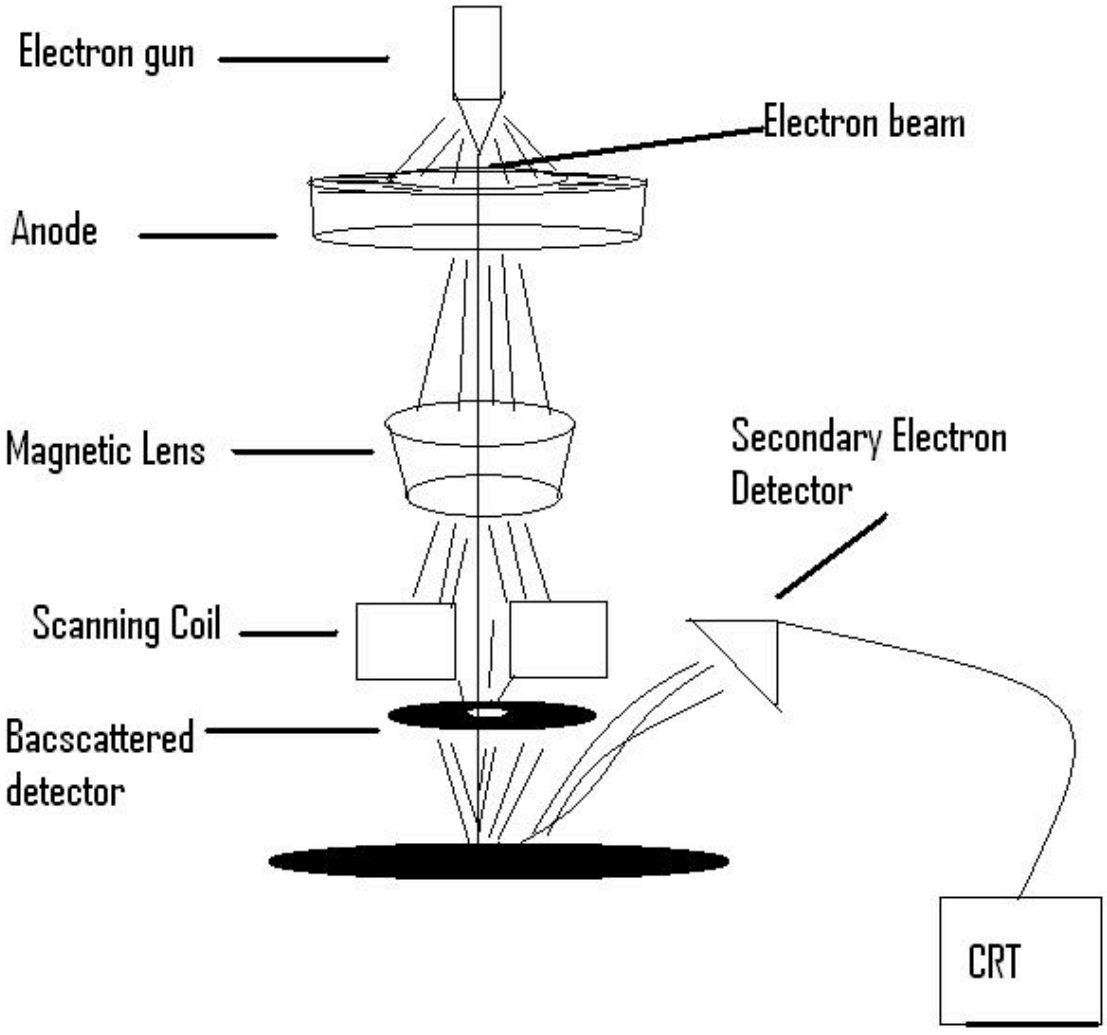


Simplified figure showing the scanning electron microscope.

The development of the SEM was largely credited to Max Knoll of Germany. The SEM used to generated images of complete films and residues of BSA, as reported in the subsequent chapters, is the Hitachi S800 SEM. Figure 6 shows a schematic illustration of the SEM. This type of SEM is considered a field emission SEM; meaning electrons are generated from a source which has been made into a very fine point. A strong electric field between the cathode (i.e. source or electron gun) and the anode generate electrons which are accelerated towards the sample. Magnetic lens are used to control the electron beam spreading as well as electron current onto the sample. Scanning coils deflect the electron beam and make a raster pattern on the surface. Therefore, magnification can be achieved by controlling the scanning coils to generate a smaller raster pattern. Because the electron beam is sensitive to changes in electric and magnetic field, the electron beam and sample are placed in a high vacuum system. The interaction between the electron beam and the sample surface is responsible for image generation. All SEM images shown in this text were generated by measuring the secondary electrons. The SEM provides excellent image contrast along with a large depth of field [37].

**Figure 7 - Electron beam and surface interaction [37]**

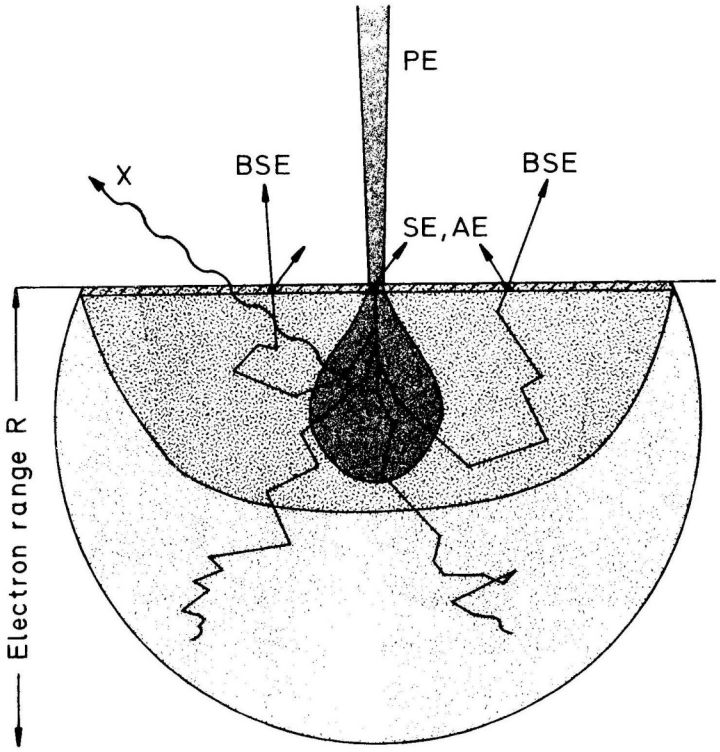


The electron beam surface interaction and resulting electrons generated from elastic and inelastic collisions.

Figure 7 shows the interaction between the electron beam and the surface that is primarily responsible for the generation of an image. Primary electrons (PE) are accelerated toward the sample surface and are a result of field emission from the electron gun. These electrons penetrate the sample surface and, as a result of elastic and inelastic scattering, cause other electrons to leave the sample with some kinetic energy. The electrons leaving the sample surface, as a consequence of electron beam (primary electrons) interaction with the surface, are of type's secondary electrons (SE), backscattered electrons (BSE), Auger electrons (AE), and x-ray quanta (X).

The SEM images shown in this text are generated by detecting the secondary scattered electrons. Secondary electrons can be easily collected by a positively biased collector grid, placed on the side, due to their relatively low exit energy of a few electronvolts [37].

The AFM is a versatile metrology tool that can be used in a variety of modes such as, magnetic force microscopy mode, thermal microscopy mode, capacitive microscopy mode, lateral force microscopy mode, lithography mode, scanning tunneling microscopy mode, and contact microscopy mode [38]. The fundamental components of the AFM are the cantilever and tip, laser, and photodiode. The cantilever, made of silicon nitride, contains a very fine tip that can be dragged across the surface. The laser beam is pointed on top of the cantilever and the reflected beam is detected by a photodiode. Deflection of the cantilever causes the beam to be reflected at a different angle as measure by the photodiode resulting in a surface image in the form of an electronic signal. The electronic signal can than be converted to an image by a computer. AFM images shown in this text were taken in the tapping mode as illustrated in figure 8.

**Figure 8 - AFM in tapping mode [38]**

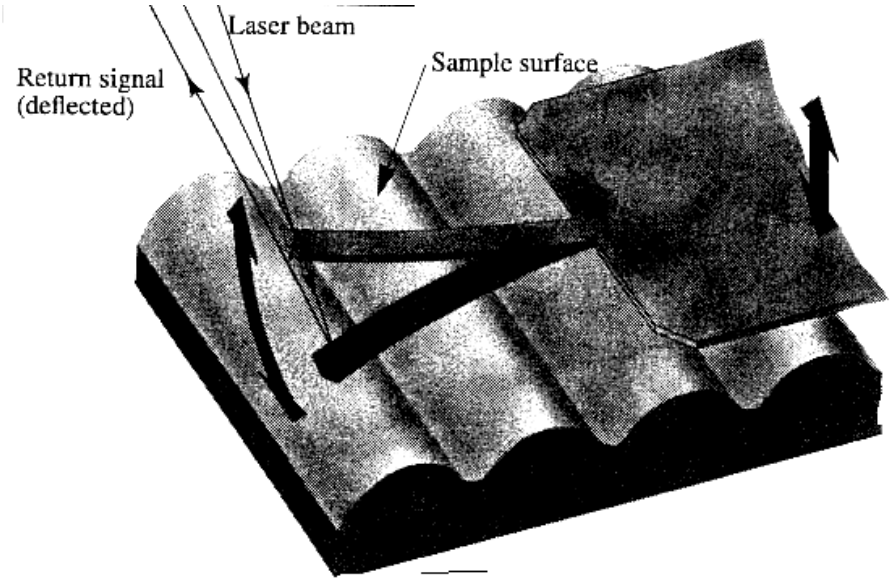


Figure illustrating the AFM cantilever moving over a sample surface during the tapping mode.

In the tapping mode, the cantilever is driven and allowed to oscillate freely in air. This generates an electronic signal as a result of changes in the angle of the beam being picked up by the photodiode. As the cantilever is brought near the sample surface, the cantilever deflects (i.e. oscillation amplitude increases or decreases) due to the force from the surface. This deflection is detected by changes in the beam pattern which changes the standard electronic signal. AFM in tapping mode is especially useful for surfaces which are soft and can damage easily [38].

Reported values of arithmetic roughness (Ra) in this text are found by equation 1 below. lx and ly are the length in the x and y directions, and f(x,y) is the surface relative to the center plane.

Equation 1- Arithmetic roughness [38]

$$Ra = \int_0^{lx}\int_0^{ly} f(x,y)dxdy$$

The mathematical expression used to calculate the average film roughness using the nanoscope software.

The subsequent sections before chapter 1 will provide background material used in the fabrication of a waveguide sandwich immunoassay biosensor. Topics will include Escherichia coli, biological tagging, the waveguide biosensor, evanescent wave, and antigen detection.

**Escherichia coli**

**Figure 9 - Escherichia Coli SEM image [39]**

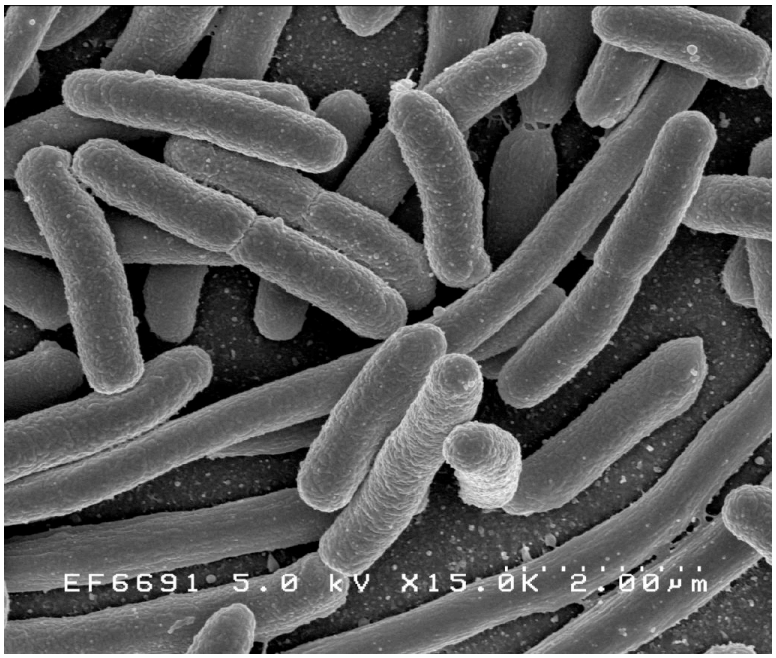


SEM image at 1500x showing the E. coli bacterium.

Figure 9 shows an SEM image of Escherichia coli (E. coli) bacterium at magnification 1500x [39] . Theodor Escherich, of Germany, born in 1857, was credited for discovering E. coli in 1885 as cited in his publication *The intestinal bacteria of neonates and their relationship to the physiology of digestion* [40].The scientific classification for this bacterium is as follows: the domain Bacteria, the phylum Proteobacteria, the class Gamma Proteobacteria, the order Entrobacterialis, the family Entrobacteriacae, the genus Escherichia, and the species E. coli.

E. coli have dimensions of approximately 3 um length. They appear cylindrical in shape (figure 9) and propel themselves via flagella. E. coli is commonly found in the small intestines of certain warm-blooded animals [41]. To this day, there has been more than 700 serotypes of E. coli identified [42].E coli, of type 0157:H7 was chosen in chapter 5 as the antigen for the waveguide sandwich immunoassay biosensor experiment. This strain of E. coli, often used in research labs, is considered a public health hazard. E. coli of this type can produce the harmful Shiga Toxin.

The Shiga Toxin is primarily responsible for producing illness in humans. Symptoms often include bloody diarrhea and mild fever[41]. Often, the ones most severely affected by E. coli infection are the very young and very old, especially in developing countries. According to the mayo clinic, approximately 70,000 people fall ill each year due to E. coli infection [43]. Figure 10 shows the three dimensional computer generated model Shiga toxin protein in its naturally assumed spatial configuration.

**Figure 10 – Shiga Toxin model [44]**

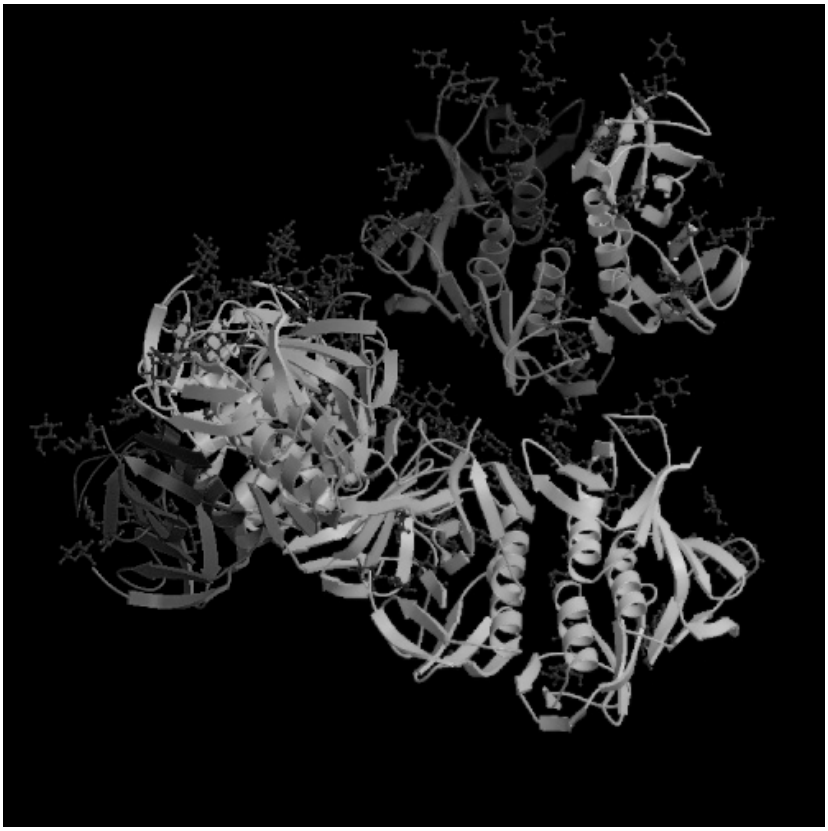

Computer generated three dimensional model showing the Shiga toxin.

## Phosphate Buffered Saline

Phosphate Buffered Saline (PBS) is commonly used in many biological applications to regulate pH and provide a so called natural environment of proteins such as antibodies. It is a mixture of a buffer and salt and provides an isotonic environment for proteins and other biological organisms. In chapter 5, PBS is used prior to exposing the microscope slide (waveguide) to the antigen E coli. In this case the PBS solution is composed of 0.01 M sodium phosphate and 0.01 M sodium chloride buffer. It is well known that functionally active proteins are sensitive to changes in pH and may denature.

**Total internal reflection**

Equation 2 – Snell's law

$$N_1 SIN\theta_1 = N_2 SIN\theta_2$$

Equation 3 – Critical angle

$$\theta_c = SIN^{-1} (N_2/N_1)$$

A review of Snell's law is required prior to the discussion of total internal reflection and evanescent waves. Equation 2 mathematically describes Snell's Law. $N_1$ and $N_2$ are the refractive indices of the two mediums. Both $\theta_1$ and $\theta_2$ are measured normal to the plane of incidence. Figure 11 shows the refraction of a wave from a denser medium towards a less dense medium. Notice that the angle of the propagation of light, as denoted by the arrowed lines, changes at the interface; the light refracts hence some of the light is reflected back. The minimum angle at which all light it totally internally reflected back is termed the critical angle, as denoted in equation 3. When the incidence angle is greater than the critical angle, an electromagnetic wave propagates through the interface despite the total internal reflection of light. This electromagnetic wave is given the name evanescent wave.

**Figure 11 – Illustration of Snell's law [45]**

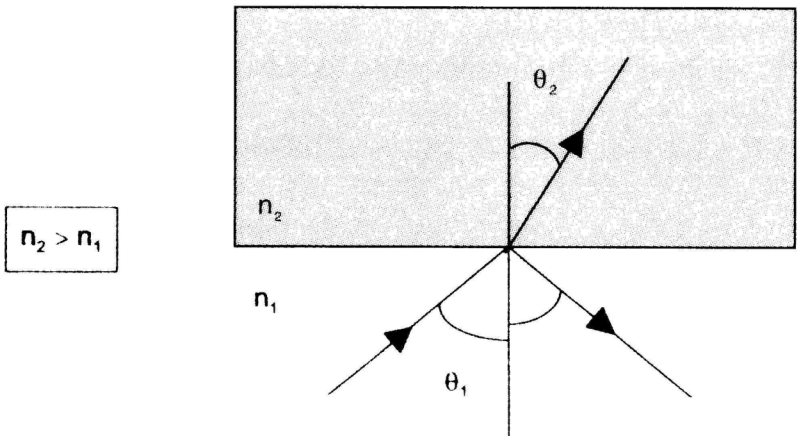


Illustration showing the refraction of light using Snell's law from a dense medium to a less dense medium.

The evanescent wave was first described in 1965 by Hirschfeld [46]. The penetration depth of the evanescent field into the second medium is on the order of 100 nm and decays exponentially. Equation 4 and 5 shows the exponential nature of the evanescent wave in the second medium. $I_Z$ is the evanescent field intensity away from the interface. $I_O$ is the evanescent wave intensity at the interface and $Z$ is the distance away from the interface. $D_P$ refers to the penetration depth of the field and is determined using equation 5. In equation 5, $\lambda$ is the wavelength of light, $N_1$ and $N_2$ are the refractive indices of the mediums, and $\Theta_1$ is the angle of incidence.

Equation 4 – Evanescent field

$$I_Z = I_O EXP^{-Z/D_P}$$

Equation 5 – Penetration depth

$$D_P = \lambda / (4\pi \, SQRT \, (N_1^2 SIN^2 \Theta_1 - N_2^2)$$

Figure 12 is a graph showing the exponential decay of the evanescent wave. The y- axis shows the ratio the intensity of the evanescent field at some distance away from the interface over the intensity of the evanescent field at the interface. The x-axis shows increasing distance (z) from the interface. The penetration depth at 1/e is denoted as *Dp*. The exponential behavior of the evanescent wave is exploited in many devices. Such devices include resonant mirrors, interferometers, surface plasmon resonances sensors, and fiber optics and planar array fluorescence biosensors[47] .

**Figure 12 –Evanescent field intensity versus distance [48]**

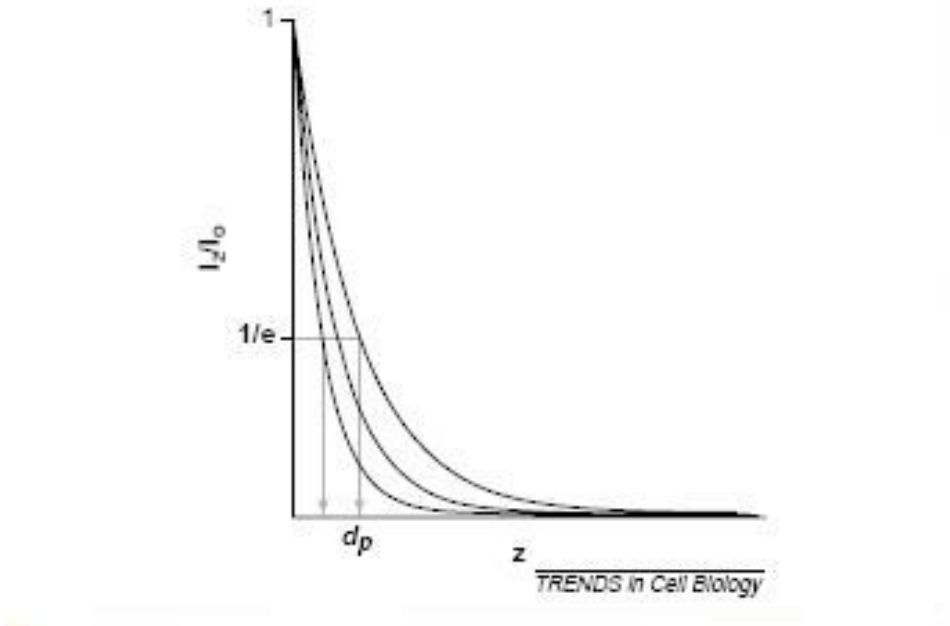


Graph showing the evanescent field decay versus distance from the interface.

In chapter 5, a description of the fabrication of a sandwich immunoassay biosensor based on waveguide technology will be discussed. A waveguide simply serves to direct light in some direction. For the device described in chapter 5, the microscope slide it self acts as a waveguide. A laser is shot into the end of the microscope slide so that the laser light will be evenly distributed along the length of the slide. Figure 13 shows the dependence of evanescent field strength on the angle of incidence. Therefore, determining the correct angle so as to maximize the evanescent field strength is important for efficient detection of E. coli.

As seen in the figure, the closer the incidence angle is to the critical angel, the more intense the resulting evanescent wave becomes. Note the HLAB 5000 detection device, as described in the subsequent section, has taken this into account.

**Figure 13 - Evanescent field strength and angle of incidence [49]**

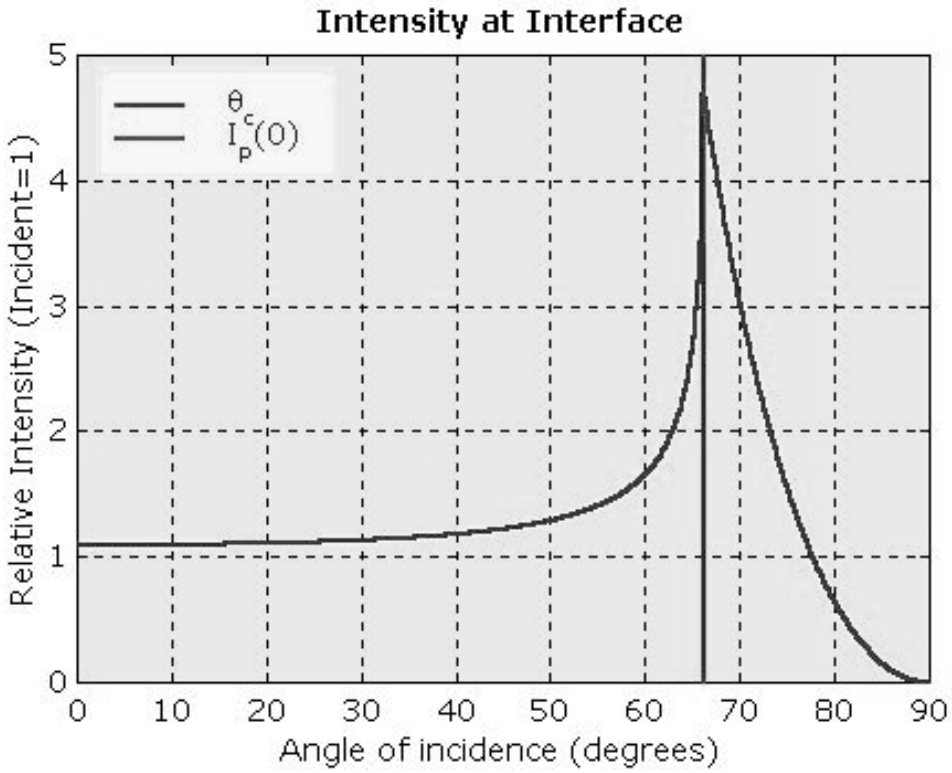


graph illustrating the evanescent wave intensity dependence on the critical angle.

**The waveguide biosensor**

An E.coli waveguide biosensor was fabricated (chapter 5) using the airbrush deposition technique. The deposition parameters were chosen as a result of the experiments described in chapters two, three, and four. Fabrication of the waveguide using the airbrush technique demonstrated the versatility of this deposition methodology.

Many have cited D. M. Frazer's definition of a biosensor which states, "A biosensor is an analytical device incorporating a deliberate and intimate combination of a specific biological element and physical transducer" [50]. Biosensors were first reported in the early 1960's [51]. Today, biosensors are applied in a variety of fields such as, agriculture [52], clinical [53], environmental [54], and biotechnology [55], among many others. Modern biosensors provide rapid and affordable interrogation as opposed to conventional techniques like chromatography, spectrophotometery, electrophoresis, and titration [56]. Biosensors take advantage of a plethora of molecular recognition elements such as enzymes, antibodies, receptors, organelles, microbes, animal and plant cells and tissues [57].

**Figure 14 - Steps for sandwich immunoassay**

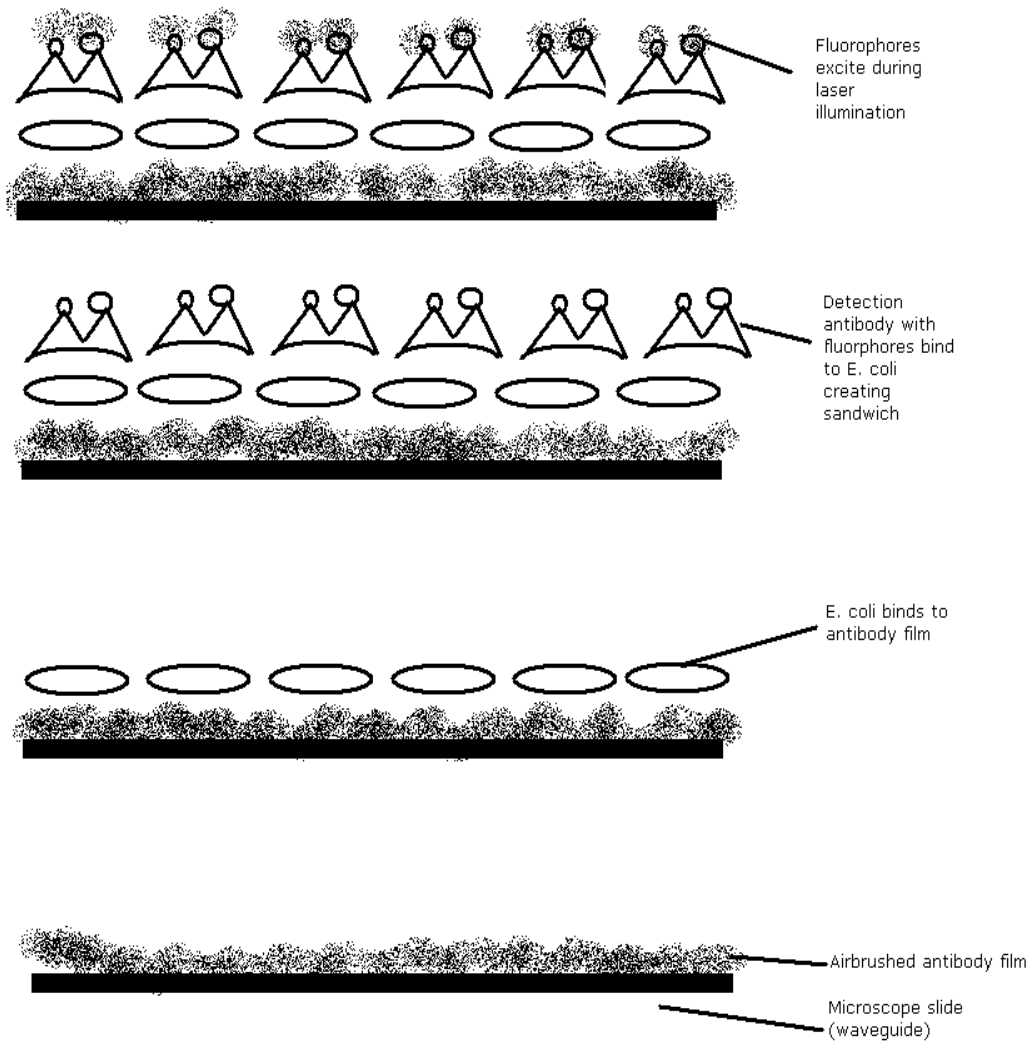


Illustration shows the steps of a sandwich immunoassay. Antibody film is first airbrushed onto a microscope slide (waveguide). E.coli binds to antibody film, upon which the tagged detection antibody binds to E. coli (creating *sandwich*) Fluorophores fluoresce upon excitation of a specific wavelength of light.

The biosensor fabricated in chapter 5 is a waveguide biosensor that takes advantage of the specificity of the bond between the antibody and antigen (E. coli) resulting in a sandwich immunoassay. Many applications of the waveguide technique

have been developed [59-63]. Figure 5 illustrates the method for detection of the E. coli antigen. The microscope slide itself acts as the waveguide upon which a thin film of E.coli antibody is immobilized by airbrush deposition. Next, the microscope slide is exposed to the environment where antigen capture occurs. The bond between the antigen and antibody may be understood as similar to a lock and key [64]. After exposure to the environment the slide is washed with PBS and weak bonds (i.e. contamination or other proteins) are washed away leaving behind only the captured antigen (E. coli). Finally, the microscope is exposed to detection antibody (creating the *sandwich* immunoassay) which binds to the E. coli antigen. The detection antibody is biotinlated with a functional group that fluoresces upon excitation of certain wavelength of light.

**Figure 15 - General schematic for antigen detection**

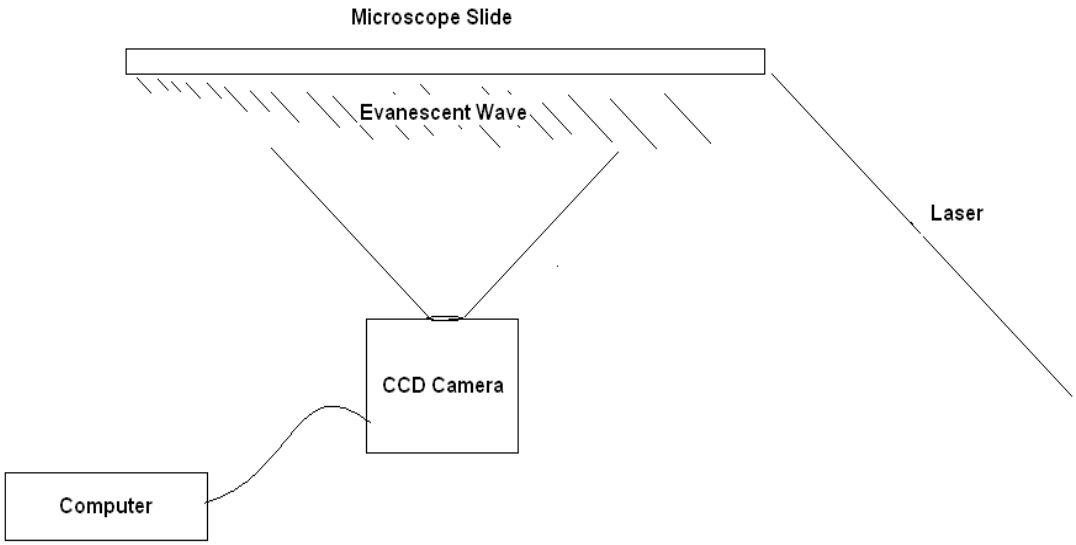


Simplified schematic illustration of the antigen detection process using the HLAB5000.

Figure 15 shows a simplified schematic for detection of antigen capture. The amount of florescence is detected by a CCD camera and an image is generated representing E coli capture. Fluorescence of the detection antibody is a result of the evanescent wave generated by pointing a 635 nm laser onto the proximal end of the microscope slide. The laser beam is directed onto the glass slide in such a way that the resulting incidence angle is greater than the critical angle as determined by Snell's Law. Even though all the light is reflected, an electromagnetic wave propagates in parallel to microscope surface for approximately 100 nm [65]. This wave can then be used to excite molecules very near to the surface of the microscope slide.

# Chapter 2

In chapter 2, the spray parameters carrier gas pressure, intake valve opening, airbrush to substrate distance, and concentration of spray solution examined via AFM and SEM analysis. Prior to droplet size and roughness analysis, the rate of spray related to carrier gas pressure and intake valve opening was determined. Next, the droplet size dependency on the spray parameters was investigated for each the airbrush parameters. Finally, the average roughness of complete films was determined against the four airbrush parameters.

## Spray rate

Initial airbrush experiments focused on understanding the spray rate relationship between intake valve setting (thumbwheel rotations) and carrier gas pressure. The airbrush curves generated as a result of this investigation allowed for the calculation of deposition times in subsequent sections.

First, the spray rate versus intake valve opening was investigated, the results of which are shown in the right graph of figure 16. For this experiment the carrier gas pressure was held at 30 psi, while the number of thumbwheel rotations was varied

between 0.5 and 5 rotations. A mixture of ACN and DI water, in a ratio of 4:1, was placed into the airbrush solution container and the time needed to spray 10 ml of this solution was recorded. This procedure was repeated 10 times and an average rate of spray along with the standard deviation was found. Note the error bars indicate one standard deviation. The resulting graph suggests that the spray rate increases non-linearly from 20 μl/sec to 100 μl/sec as the intake valve is varied between 0.5 and 5 thumbwheel rotations. The standard deviation of spray rate for each point appears to be approximately 20 % likely a result of tolerances in the intake valve mechanism. This suggests that for precise control of deposition rates a low to medium intake valve opening should be employed.

Next, spray rate versus carrier gas pressure was investigated as shown below in the left graph of figure 16. For this experiment the thumbwheel was held at 3.5 rotations, while the carrier gas pressure was varied in four steps from 10 to 60 psi. Similarly, a change in volume analysis was conducted and an average spray rate and standard deviation were calculated. As the graph suggests, the spray rate appears to linearly increase within error from 10 μl/sec to 40 μl/sec as the carrier gas pressure was varied between 10 and 60 psi. Again, the spray rate error appears to be approximately 20 % and is likely a result of the same tolerances in the intake valve mechanism as was observed in the intake valve spray rate experiment (figure 16 a).

**Figure 16 - Airbrush calibration curves**

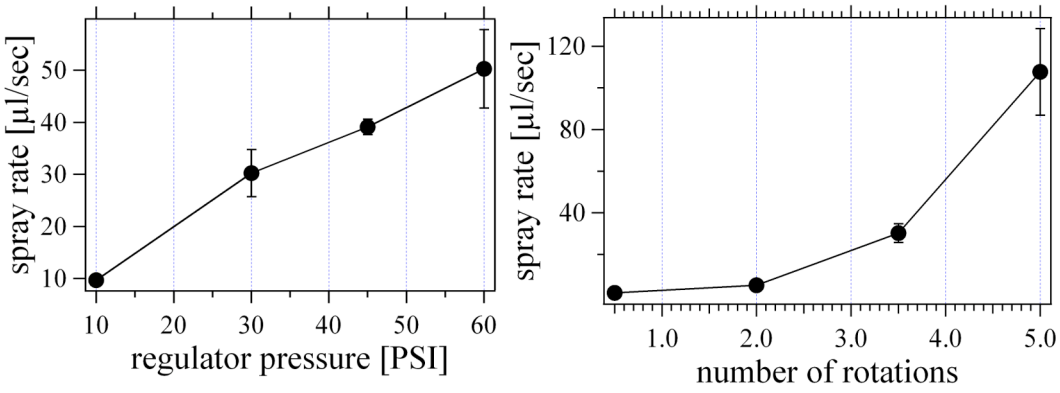


Gas pressure and solution intake valve setting influence on the spray rate. Error bars indicate one standard deviation.

**Droplet size**

Figures 17-20 summarize the results of the droplet size dependence on carrier gas pressure, intake valve setting (thumbwheel rotations), distance between the airbrush and substrate, and the BSA concentration of the spray solution. Each figure shows SEM images at magnification 1000x, corresponding to its droplet diameter data point. Scratch marks were made on the surface to provide a clear contrast between the BSA residues and the silicon substrate. Droplet size dependence was assessed by measuring the outer diameter of dried droplet residues on the surface using SEM analysis and standard statistical methods. The deposition times were determined using the airbrush calibration curves (figure 2) and some trial and error, as individual droplets were necessary for quantification.

**Figure 17 - Ring diameter versus carrier gas pressure**

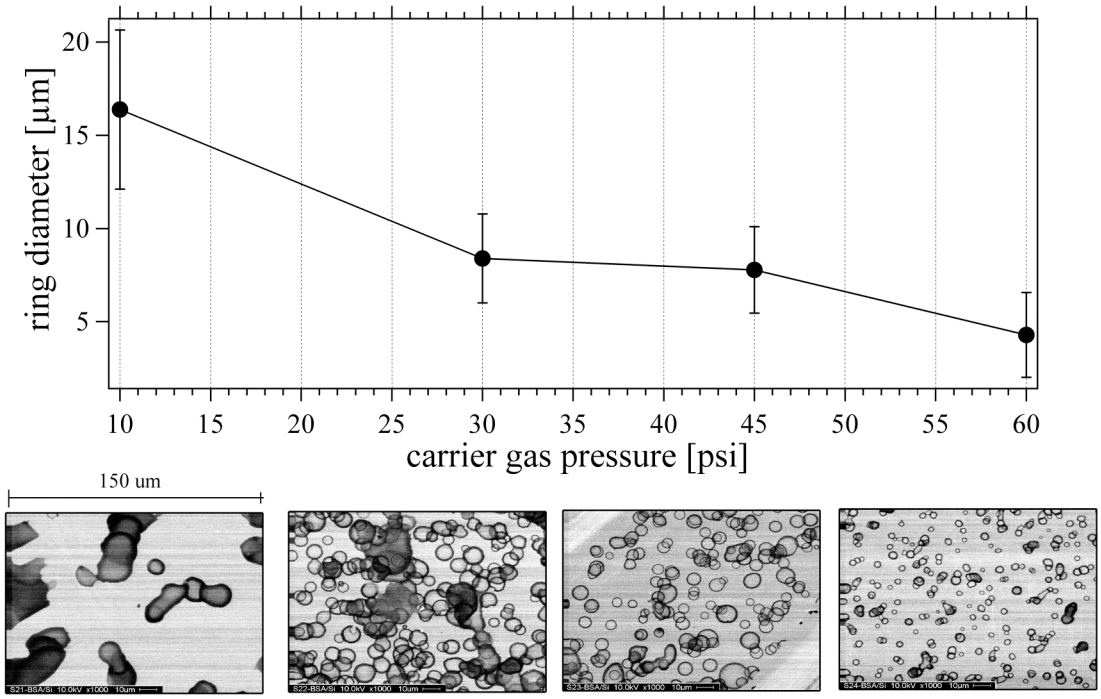


Droplet size dependence on carrier gas pressure. Droplet size was estimated from the diameters of residues (ring diameter) as characterized via SEM. The SEM images (magnification 1000x) used for evaluation are shown below corresponding to each of the data points. Each image to scale is 150 um wide as indicated by the scale bar.

Figure 17 shows the effect of carrier gas pressure on the average ring diameter. The carrier gas pressure was varied four times, while the intake valve setting (3.5 thumbwheel rotations), distance between the airbrush and substrate (20 cm), and BSA concentration were held constant (1 mg/ml). The deposition time for each data point (left to right) was 55, 18, 14, and 11 seconds. As the graph suggests, average droplet size decreased with increasing carrier gas pressure. The smallest average ring diameter (5um) was achieved at 60 psi. Coalescence of residues was observed at 10 psi as a result of poor

atomization resulting in large droplets on the surface. As carrier gas pressure was increased the amount of coalescence observed was reduced since smaller droplets evaporated before subsequent droplets arrived.

**Figure 18 - Intake valve opening and ring diameter**

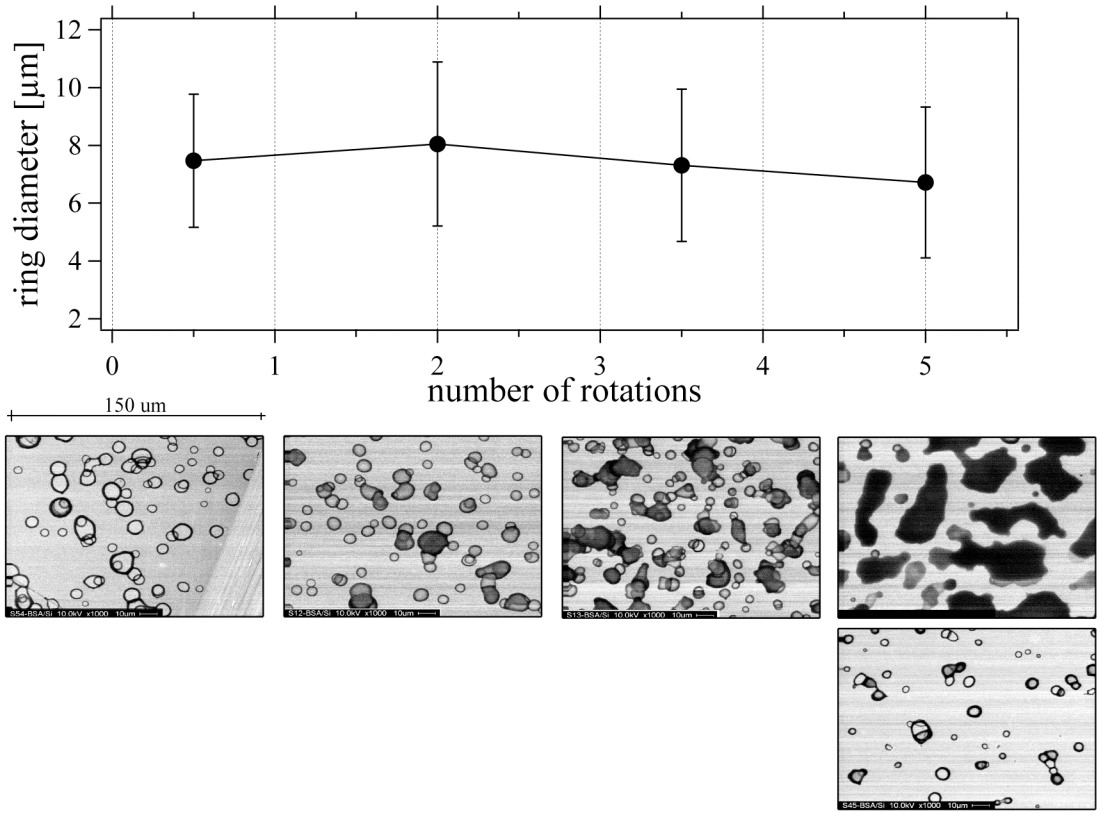


Droplet size dependence on number of rotations. Droplet size was estimated from the diameters of residues on the surface. The error bars indicate 1 standard deviation. SEM images shown at magnification 1000x. Each SEM image has a width of 150 um to scale.

Figure 18 shows the droplet diameter dependence on intake valve opening (thumbwheel rotations). The thumbwheel controls the intake valve opening which in turn controls the amount of solution injected into the carrier gas stream. The carrier gas

pressure was held at 30 psi, while the number of thumbwheel rotations was varied between 0.5, 1.5, 3.5, and 5 rotations. The deposition times were 342, 103, 18 and 5 sec, respectively. The airbrush to substrate distance was fixed to 20 cm and the solution concentration used was 1 mg/ml. SEM images are shown below that graph corresponding to each data point. As the graph illustrates, the droplet diameters varied between 6 and 8 μm and the standard deviation appears to be fairly constant over the examined range. Upon further examination of the SEM images, increased coalescence appears to occur as the intake valve setting is increased. Note that the amount of deposited material was kept constant, within error. At five thumbwheel rotations individual droplets were no longer able to be distinguished. Therefore, a short deposition of 2 sec was performed and used for the calculation of the 5 rotation data point. It is apparent after this experiment that the intake valve opening has little influence on the diameter of dried droplet residues. This point is further supported upon examination of the 0.5 rotation sample, where superimposed droplet residues are observed without coalescence as a result of individual droplets drying before subsequent droplets arrive.

**Figure 19 - Ring diameter versus solution concentration**

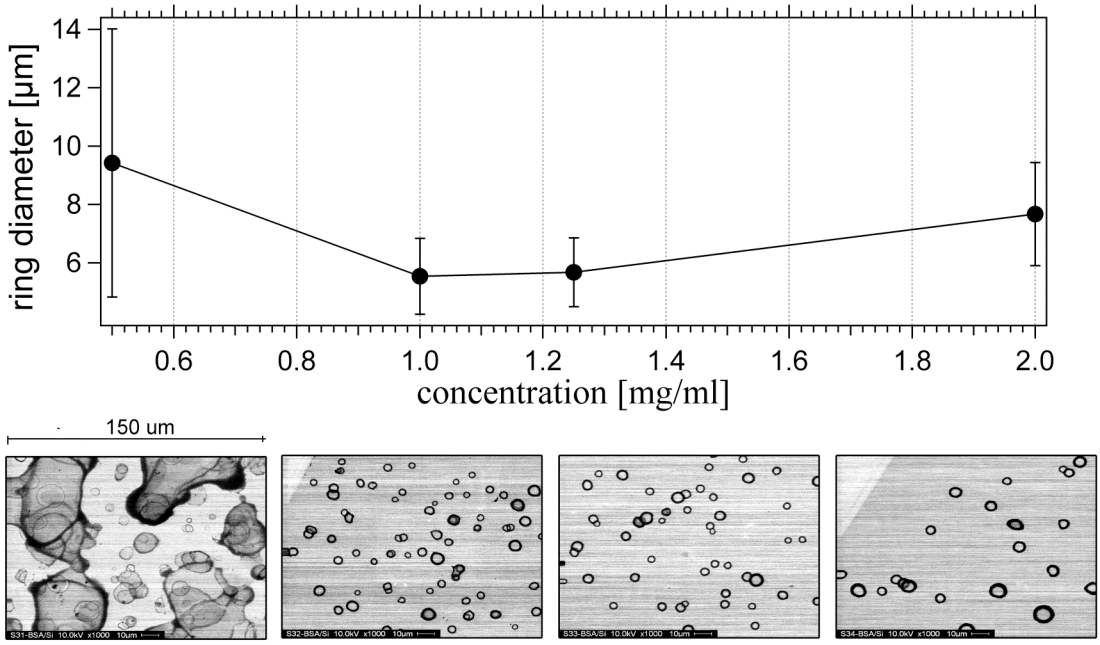


Droplet size dependence on solution concentration. Droplet size was estimated from the diameters of residues as characterized via SEM. The SEM images (magnification 1000x) used for evaluation are shown below corresponding to each of the data points. The concentrations investigated were 0.5,1,0.25, and 2 mg/ml. Each SEM image is scaled to 150 µm width.

Figure 19 shows the droplet diameter dependence on the BSA concentration. The carrier gas pressure was fixed at 30 psi, while the concentration of solution was varied from 0.5 to 2.0 mg/ml. 2.0 mg/ml was the highest concentration used as attempts to create higher concentrations resulted in precipitation. The intake valve opening was set to 3.5 rotations and the airbrush to substrate distance was fixed to 20 cm. The deposition times were (35, 18, 12, and 8 sec) varied reciprocally with the concentration to keep the amount of solution deposited roughly the same for each sample. As depicted in the graph, a slight increase in magnitude from 6 µm to 8 µm is observed. However, the averages fall

within the standard deviation suggesting the increase in ring diameter was not significant. Upon examination of the sample related to 0.5 mg/ml, coalescence was observed and was likely a result of the relatively large deposition time for this sample. Examination of the droplets around the coalesced residues suggested that no significant change in droplet size was observed.

**Figure 20 - Ring diameter and airbrush to substrate distance**

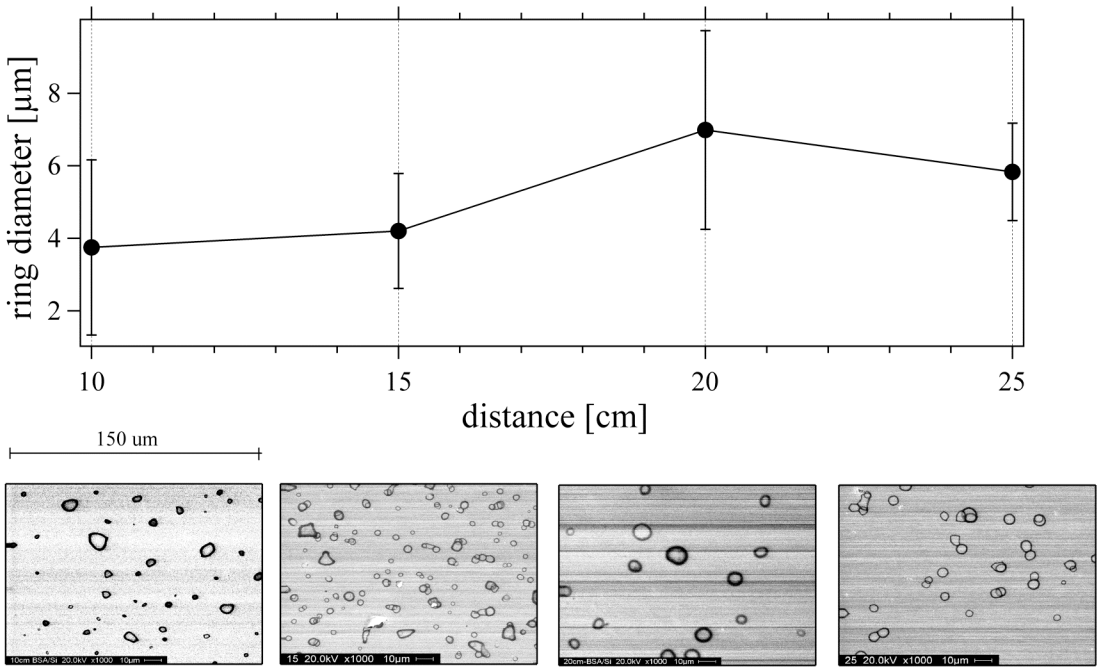


Droplet size dependence on airbrush to sample distance. The average droplet size and standard deviation (error bar) was determined by measuring dried residue diameters on the surface. SEM images are shown at 1000x. Each image is scaled to 150µm width.

Figure 20 shows the results of the distance variation series. The carrier gas pressure was fixed to 30 psi, the intake valve setting was held at 3.5 rotations, and the solution concentration was 1 mg/ml, while the distance between the airbrush and substrate was varied from 10 cm to 25 cm in four steps. The deposition times were 1, 6, 62 and 62 sec respectively. A change in procedure was required for the 10 cm data point, as residue coalescence made it difficult to distinguish single droplets. Therefore, short tap of the airbrush finger-level assembly was used to allow for single droplet residues to be observed for statistical analysis. As evident in the graph, droplet residue size does not change significantly through the distance examined as averages fall within the standard deviations.

In summary, droplet size in mainly influenced by carrier gas pressure. Increasing the carrier gas pressure serves to reduce average droplet size and amount of coalescence. A high deposition rate results in increased coalescence and affects surface morphology of films, as will be discussed in the next section.

**Thin film deposition**

In this section, the spray parameters enabling smooth thin film deposition was investigated. The SEM images in figure 12 show the formation of a continuous BSA thin film. Five samples were prepared and the deposition times were varied from 10 to 50 sec in 10 sec intervals. The deposition parameters for this investigation were an intake valve setting at 3.5 thumbwheel rotations, an airbrush to substrate distance of 20 cm, a carrier gas pressure of 30 psi, and 1 mg/ml BSA concentration. The film seems to grow droplet by droplet stacking one on top another while some coalescence occurs. Complete films tend to be composed of ring like structures as a result of droplet evaporation.

**Figure 21 - Thin film formation**

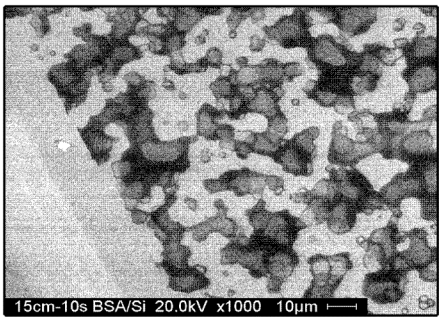


10 sec

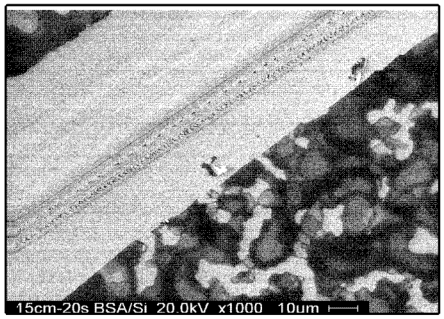


20 sec

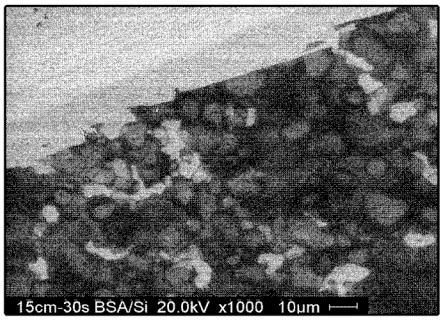


30 sec

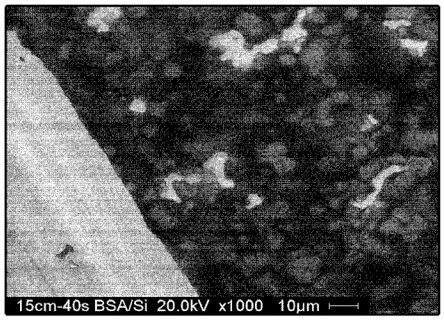


40 sec

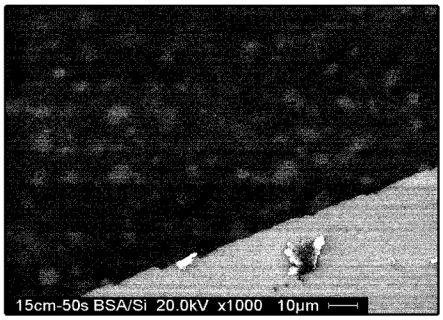


50 sec

SEM images taken at 1000x magnification showing the growth of a BSA film on a Si substrate. Five samples were made increasing the deposition time by 10 seconds. 50 seconds deposition yields as complete film.

Figures 22 – 25 show the effect of varying carrier gas pressure, airbrush to substrate distance, intake valve opening, and BSA concentration on thin film roughness and growth rate. In each of the following experiments in this section, only one parameter was varied while the other three were held constant. Deposition times were varied such that each sample would have approximately the same average film thickness. Each data point represents the average of three films. Below the graph, SEM (1000x) and AFM (80 μm x 80 μm) images are shown corresponding to each data point and represent a typical film. Scratch marks were made through the film to provide a clear contrast between the film and substrate. AFM analysis was performed on each sample at roughly the center of each film. Growth rate calculations were determined by performing a step height calculation at the scratch mark and then dividing by the deposition time.

**Figure 22 -Roughness and growth rate versus carrier gas pressure**

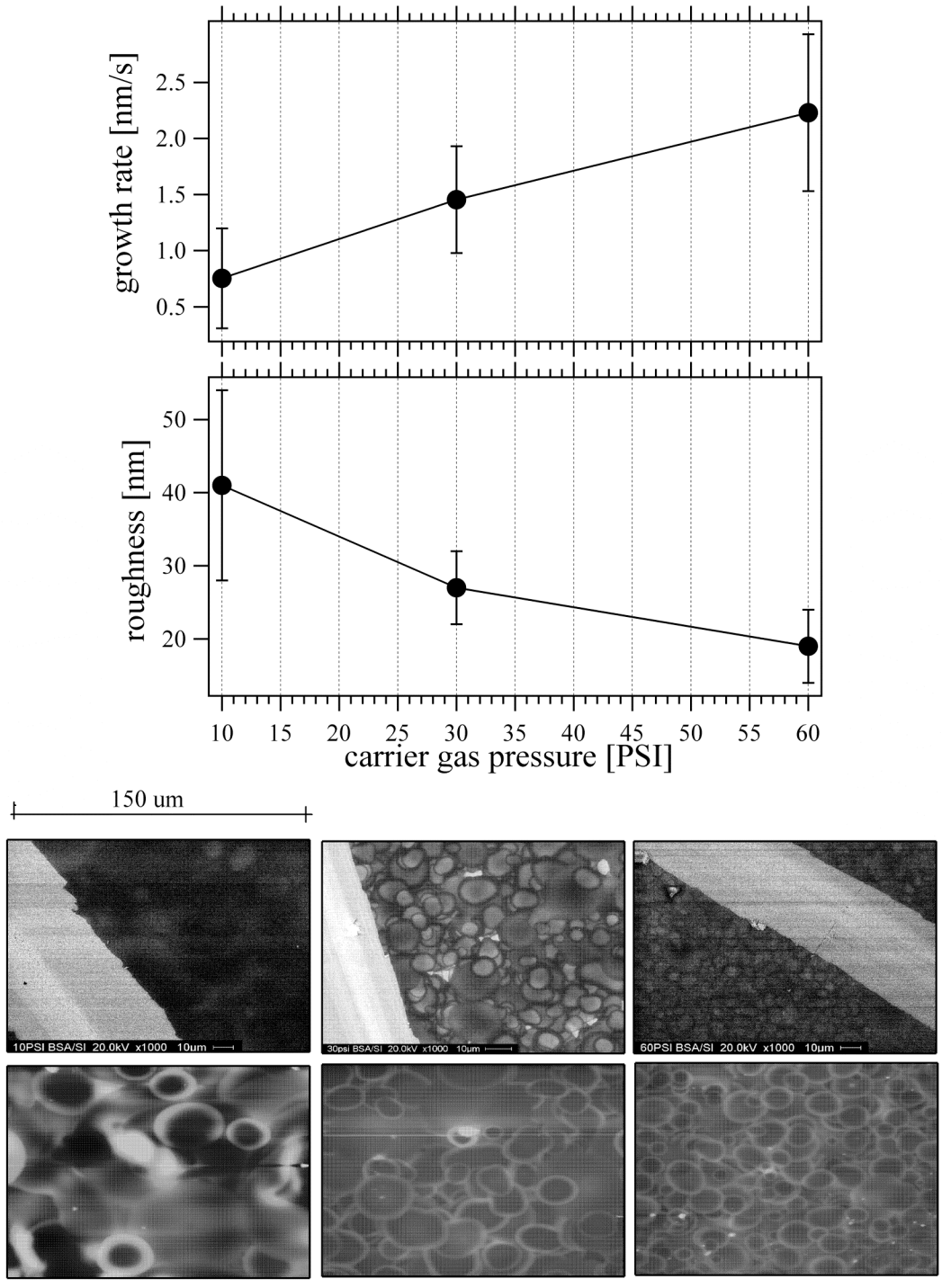


Roughness and growth rate dependence on the carrier gas pressure. The SEM image shown at 1000x and AFM (700nm scale) is of area 80 x 80 $\mu m^2$. Fixed parameters: 15 cm, 3.5 rtn, 1 mg/ml. The size bar indicates 150 µm width for each SEM image.

Figure 22 shows the effect of carrier gas pressure on film roughness and growth rate. The carrier gas pressure was varied (10, 30, 60 psi) in three steps while the deposition times were varied (127, 50, and 27 seconds) such that each film would have approximately the same thickness. Increasing carrier gas pressure appears to decrease film roughness, consistent with the smaller droplet size at higher pressure. The highest average roughness was determined to be 41 nm ± 13 nm at 10 psi. The lowest average roughness observed, at 60 psi, was determined to be 19 nm ± 5 nm. At 30 psi the average roughness recorded was 27 nm ± 5 nm. The AFM (700nm height scale) images also illustrate a reduction in roughness as carrier gas pressure is increased. The growth rate increased linearly as carrier gas pressure was increased.

**Figure 23 - Distance versus roughness and growth rate**

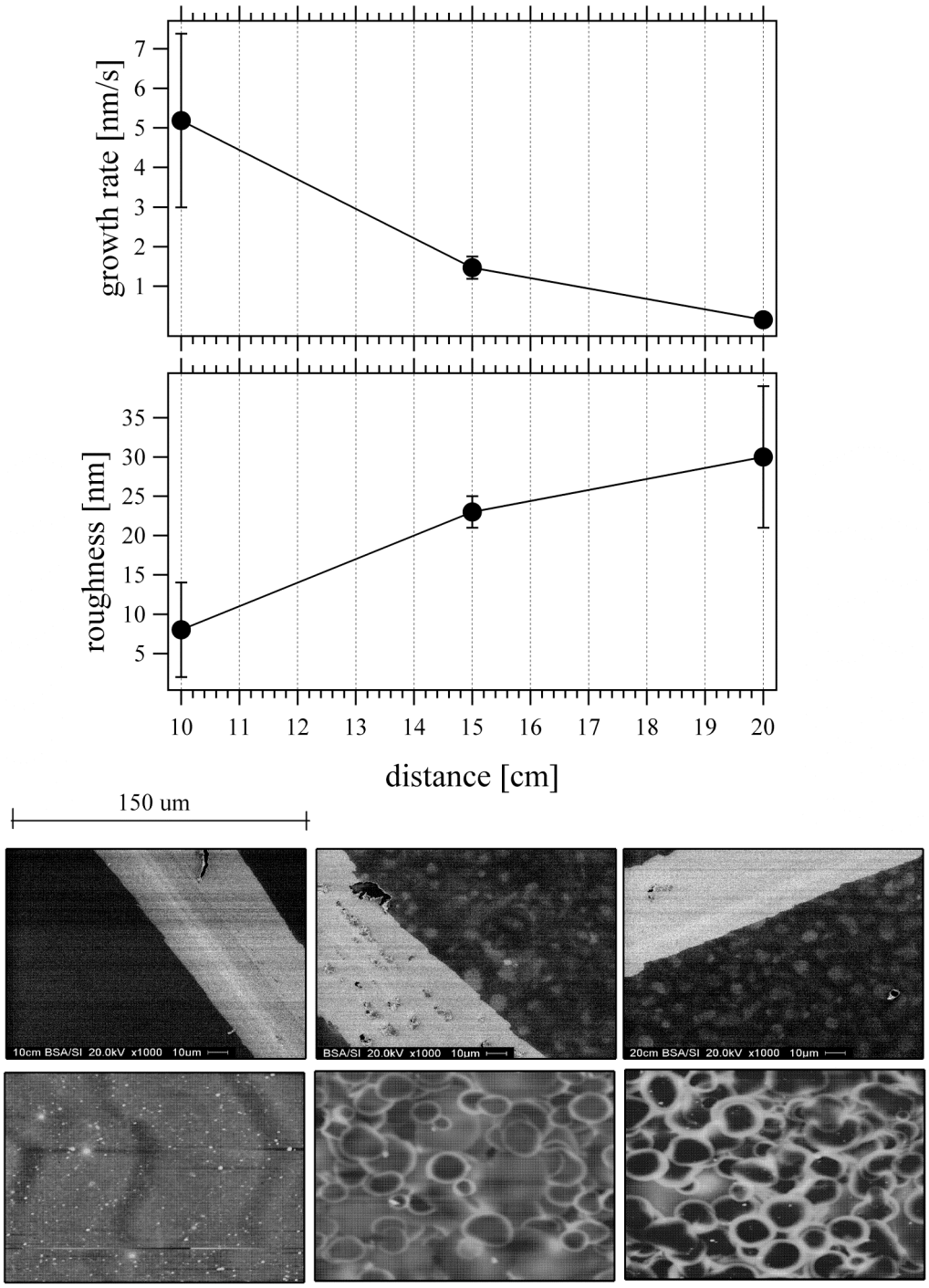


Roughness and growth rate dependence on the airbrush sample distance. The SEM images (magnification 1000x) used for evaluation are shown below corresponding to each of the investigated distances (10, 15, and 20 cm). The fixed parameters were 30 psi, 1 mg/ml, 3.5 rtn. AFM (100nm scale) is of area 80 x 80 $\mu m^2$. Note the AFM scale for sample related to 10 cm is 30 nm. Size bar indicates 150 microns for SEM images.

Figure 23 illustrates the effect of airbrush to substrate distance on roughness and growth rate. The distance was varied (10, 15, 20 cm) in three steps, along with the deposition times, such that each sample had roughly (12, 50, 127 sec) the same film thickness. As suggested by the graph, reducing the distance between the airbrush and substrate serves to reduce film roughness and increase growth rate. The improvement in roughness, as the distance between the airbrush and substrate is reduced, is likely a result of surface wetting. Distance reduction results in larger volumes of solution deposited in shorter times, as seen in figure 20. A smoother film is created through redissolution of previously deposited solute on the surface, as confirmed by the AFM and SEM images. The film roughness decreases from 30 nm ± 10 nm to 8 nm ± 6 nm as the distance between the airbrush and substrate decreases from 20 cm to 10 cm. Note the AFM image related to the 10 cm sample has a height scale of 100 nm, whereas the other two are shown with a height scale of 400 nm.

**Figure 24 - Roughness and growth rate versus intake valve opening**

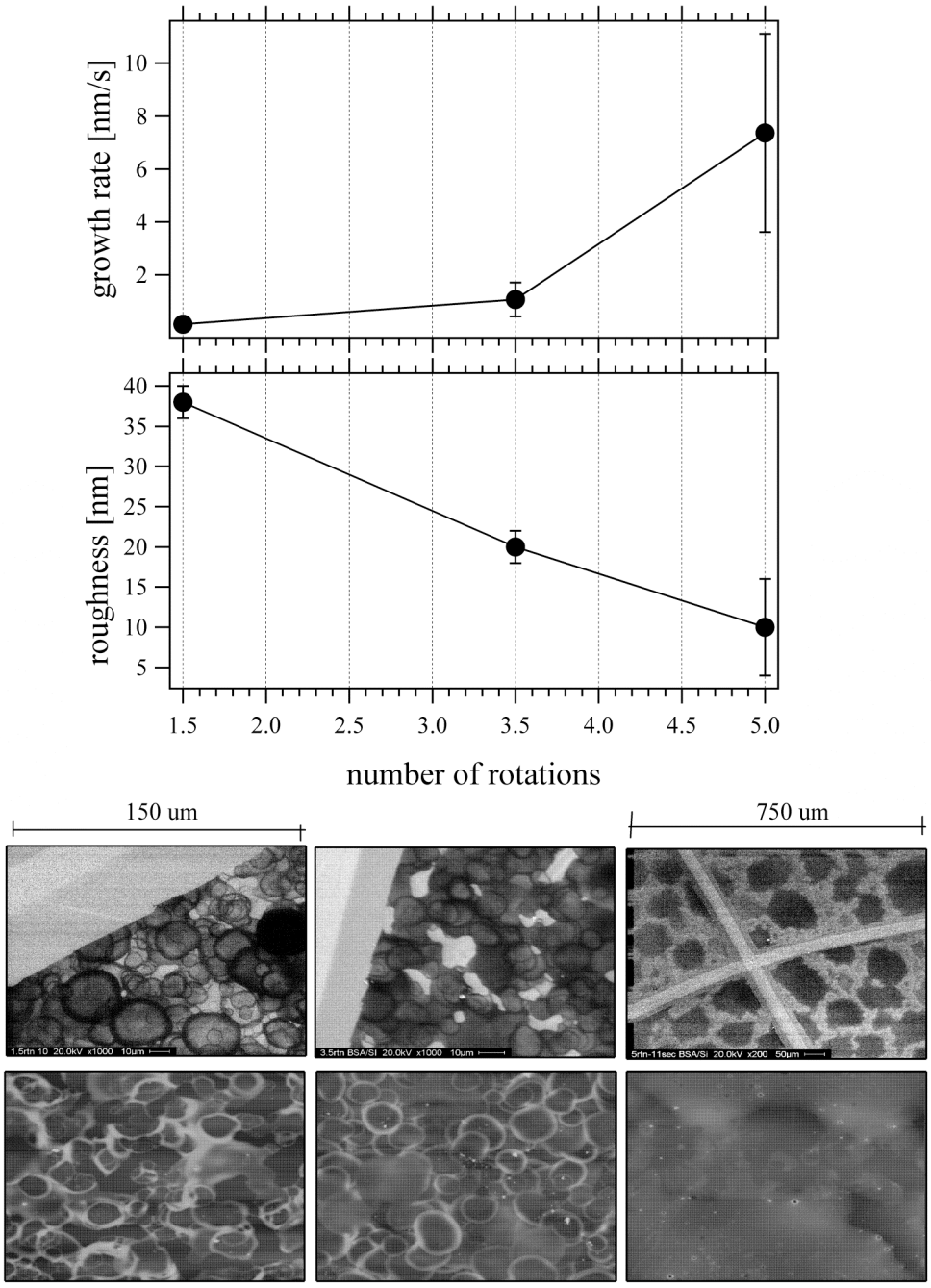


Roughness and growth rate dependence on the solution intake valve setting. The SEM images (magnification 1000x, 150 μm) used for evaluation are shown below corresponding to each of the investigated settings (1.5, 3.5, and 5.0 rotations). Note the SEM image related to 5 rtn is 200x and has 750 μm width. AFM (500 nm scale) is of area 80 x 80 $\mu m^2$

Figure 24 shows the effect of opening the intake valve on the roughness and growth rate of BSA films. For this series the deposition parameters were 30 psi carrier gas pressure, 15 cm airbrush to substrate distance, and 1 mg/ml BSA concentration, while the intake valve setting (1.5, 3.5, 5 rtn) was varied and the deposition times ( 900, 50, 27 sec) for each sample were adjusted such that each sample had roughly the same average film thickness. At 1.5 thumbwheel rotations a roughness of 39 nm ± 3 nm was achieved. At 3.5 thumbwheel rotations an average roughness of 21 nm ± 2 nm was found. A significant drop in roughness was observed at 5 rotations where the average surface roughness was determined to be 10 nm ± 7 nm. Opening the intake valve does not appear to affect the droplet size (figure 18), however opening intake vale (increasing the number of thumbwheel rotations) does increase the amount of solution injected into the carrier gas stream. At low flow rates (1.5 thumbwheel rotations), complete films are composed of ring like residues as a result of droplet evaporation before subsequent droplets arrive. As the solution flow was increased (3.5 thumbwheel rotations), increased coalescence occurs and smoothens the deposit. At five thumbwheel rotations, the solution flux was so large that solution beading and run-off occurred resulting in an incomplete film. The AFM images shown below the figure have a height scale of 500 nm. Additionally, AFM roughness analysis for the samples related to five thumbwheel rotations were conducted on one of the “puddles” of BSA. Note the SEM image related to the 5 rotation sample is shown at 500x to better view film morphology. It can be concluded from this experiment that increasing the flow rate serves to increase the amount of coalescence and redissolution of residues resulting in a smoother film.

**Figure 25 - BSA concentration versus roughness and growth rate**

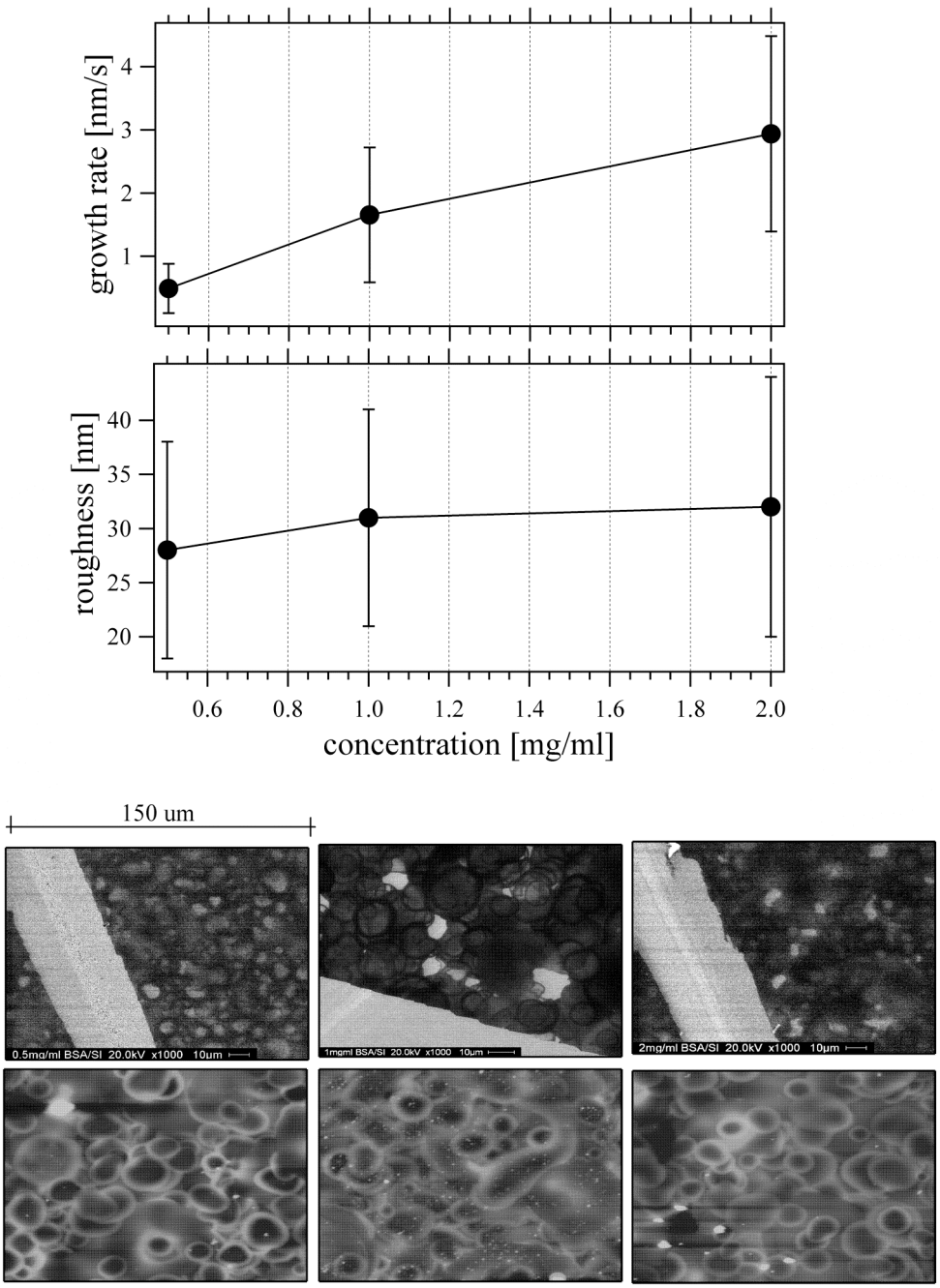


Roughness and growth rate dependence on the solution concentration. The SEM images (magnification 1000x, 150µm width) used for evaluation are shown below corresponding to each of the investigated concentrations (0.5, 1, and 2 mg/ml). The fixed parameters were 30 psi, 15 cm, 3.5 rtn. AFM (500nm scale) is of area 80 x 80 $\mu m.^2$

Figure 25 illustrated the effect of BSA concentration on film roughness and growth rate. For this series the carrier gas pressure was fixed to 30 psi, the intake valve opening was set to 3.5 rotations, and the distance between the airbrush and substrate was 20 cm, while the BSA concentration was varied from 0.5, 1, and 2 mg/ml. The deposition times were 100, 50, and 25 sec, respectively. As suggested by the graph, BSA concentration appears to have very little effect on film roughness. A slight reduction in film roughness is observed for the samples related to 0.5 mg/ml and is likely a result of increased deposition time allowing for some coalescence. As expected, the growth rate linearly increases with increasing BSA concentration. The SEM and AFM (500 nm height scale) images appear similar for all three films.

In summary, two growth regimes are observed for the airbrush deposition technique. The low flux regime, yields relatively rough films that are primarily composed of dried ring-like residues with very little coalescence. The resulting films generated by this growth mode are a product of low solution flux onto the substrate surface. In this mode, droplets completely evaporate on the surface before subsequent droplets arrive. This can be achieved by reducing the number of thumbwheel rotations (i.e. reducing the intake valve opening), increasing the airbrush to substrate distance, or by reducing the carrier gas pressure.

In the high flux growth regime, films are created as a result of high solution flux onto the substrate surface. In this mode, coalescence is observed as a result of droplets on the surface that do not evaporate before subsequent droplets arrive, resulting in a

smoother film. In the extreme case, a solution flux that is too large results in large puddle areas and solution run-off from the sample surface. As a consequence, to create smooth and complete films, the solution flux onto the surface must be high enough to allow for redissolution of residues on the surface, while not being so large as to create puddles and solution run-off from the sample. Finding the correct flux is a result of achieving a balance between the airbrush deposition parameters. Under steady-state conditions, relatively smooth and complete thick films should be achieved.

# Chapter 3

The previous chapter explored how the airbrush parameters of carrier gas pressure, intake valve opening, distance between the airbrush and substrate, and solution concentration enabled the production of smooth thin films. It was found that the solution flux onto the surface largely influenced film roughness. Smooth and complete films are created when the solution flux onto the surface is high enough to allow for coalescence to smoothen the deposit, while not being large enough to allow for the formation of puddle areas or solution run-off from the sample. Evaporation of solution from the substrate is largely influenced by the vapor pressure of the solvent. Therefore, in this chapter the effect of the vapor pressure of the spray solution on film roughness will be assed through AFM and SEM. In the last chapter, the BSA solution that was sprayed was a mixture of ACN and DI water (4:1). Two additional solvents were chosen for deposition of BSA. The first solvent is entirely water, while the second is mostly composed of tetrahydrofuran (THF). Table 1 lists the vapor pressure of solvents at room temperature. The THF-based solution was prepared by first dissolving the BSA into DI water, and then diluting with THF (4:1 THF: water) until a final concentration of 1 mg/ml was achieved.

The DI water solution was prepared by dissolving BSA into DI water to create a 1 mg/ml solution. In the previous chapter it was concluded that airbrush deposition of films fall into to principal growth regimes (i.e. low solution flux and high solution flux). Therefore the effect of vapor pressure will be investigated in both regimes.

**Figure 26 - Effect of solvent on roughness and growth rate**

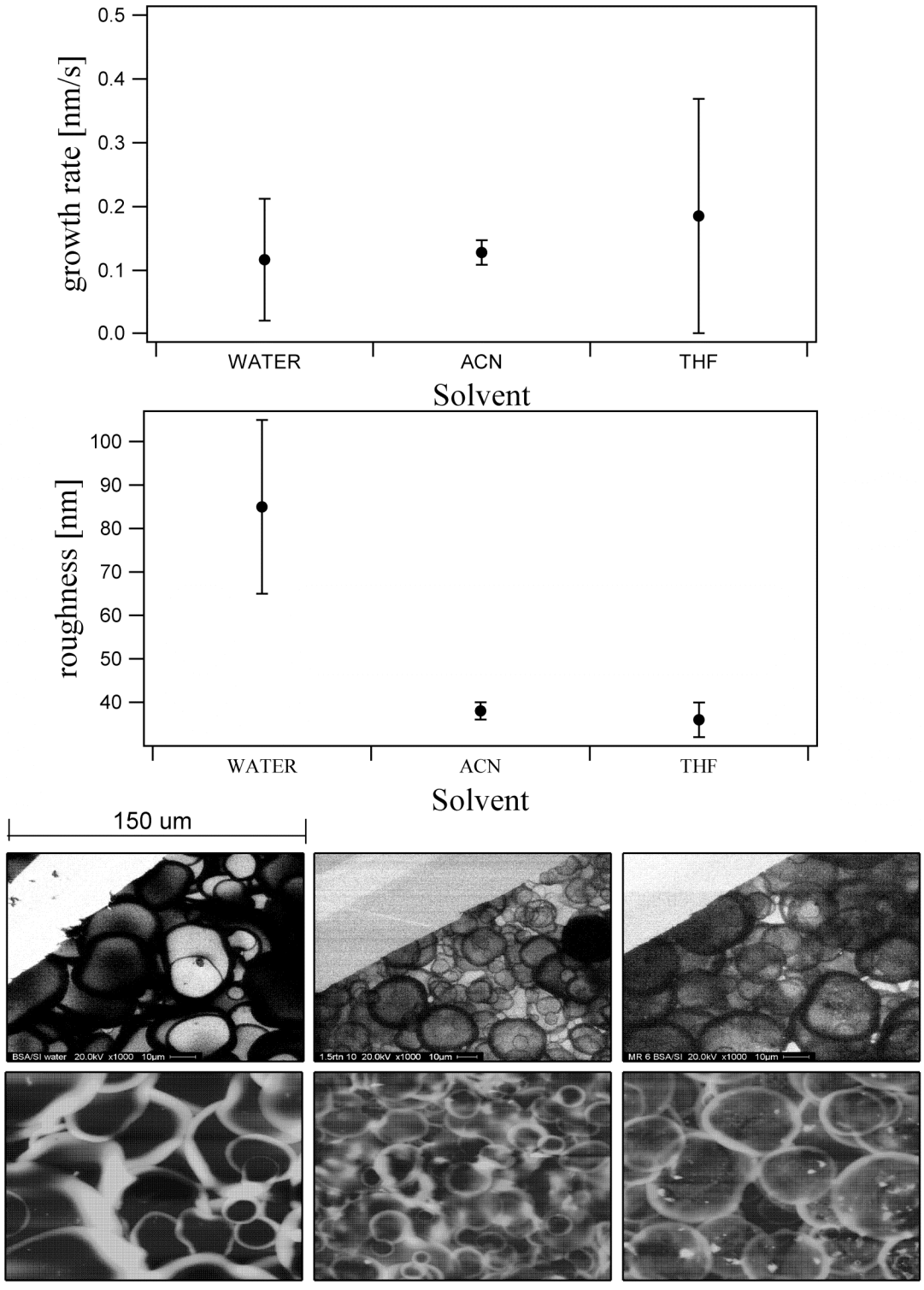


Figure shows the effect of vapor pressure of the spray solvent on average film roughness. SEM images are shown at 1000x and scale bar indicates 150 µm widths for each image. AFM (500 nm scale) is of area 80 x 80 $\mu m^2$. Fixed deposition parameters are 30 psi, 15 cm, 1 mg/ml, 3.5 rtn, and time 900 sec

**Low flux regime**

Figure 26 shows the effect of various solvents on film roughness in the low solution flux growth regime. A low solution flux onto the sample surface can be achieved by reducing the intake valve, increasing the distance between the airbrush and substrate, or reducing the carrier gas pressure. In this case, the intake valve opening was reduced. The airbrush parameters for the samples related to figure 26 are as follows: intake valve setting of 1.5 rotations, carrier gas pressure of 30 psi, an airbrush to substrate distance of 15 cm, and BSA concentration of 1 mg/ml. The deposition time for each sample was 900 sec. In this growth mode, the resulting films are relatively rough and are composed of circular residues showing little coalescence. The addition of solvent to DI water (i.e. ACN and THF in this case) increases the vapor pressure of the solution. As figure 26 indicates, a large reduction in film roughness was achieved with the presence of ACN in the spray solution. Only a slight reduction in film roughness was achieved when THF-based spray solution was used as opposed to when the ACN-based spray solution was used. The average roughness for the film created with water only was 85 nm ± 20 nm, while the average roughness for the films created with the ACN based spray solution was 38 nm ± 2 nm. The films created using the THF based spray solution yielded a measured average roughness of 36 nm ± 4 nm. Recall in figure 22, a reduction in average film roughness was observed as the carrier gas pressure was increased.

Increasing the carrier gas pressure reduces the average droplet size, as evidenced by the measuring the diameter of dried droplet residues shown in figure 17. Increased vapor pressure allows for increased evaporation (i.e. smaller droplets) before droplets impinge onto the surface. Therefore, a reduction in average film roughness is observed in the SEM images, as illustrated below.

**Figure 27 - Effect of vapor pressure on film morphology**

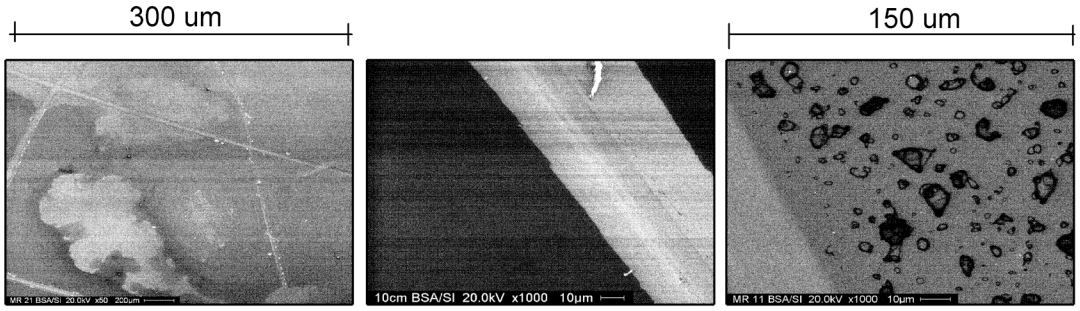


SEM images showing the effect of vapor pressure of spray solution on film morphology. Note the SEM images are shown at 50x, 1000x, and 1000x magnification with 300 µm, 150 µm, and 150µm image widths respectively. Smooth and complete films require a balance between vapor pressure and solution flux onto the sample.

**High flux regime**

Figure 27 shows the effect of solution vapor pressure on film morphology in the high solution flux growth regime via SEM images. A high solution flux onto the sample surface can be achieved by increasing the carrier gas pressure, opening the intake valve (increasing the number of thumbwheel rotations), or by reducing the distance between the airbrush and substrate. In this case, the distance between the airbrush and substrate was

reduced. The airbrush parameters for the films related to figure 27 are as follows: an airbrush to substrate distance of 10 cm, an intake valve setting of 3.5 rotations, a carrier gas pressure of 30 psi, and a BSA concentration of 1 mg/ml. The deposition time for each of the samples related to figure 13 was 12 sec. Upon examination of the SEM images, it is interesting to observe that the quality of each film appears different despite having been exposed to the same solution flux and deposition time. A vapor pressure that is too low (figure 27 a) results in the formation of puddle areas caused by solution beading and solution run-off. A vapor pressure that is too high (figure 27 c) limits the time available (due to high evaporation rate) for coalescence and redissolution of residues by solvent spreading on the surface, resulting in an incomplete film composed of large residue clusters. It can be concluded that in order to obtain smooth and continuous films (figure 27 b) the solution flux must be carefully balanced with the vapor pressure.

**Figure 28 – Effect of spray solution on growth rate and roughness**

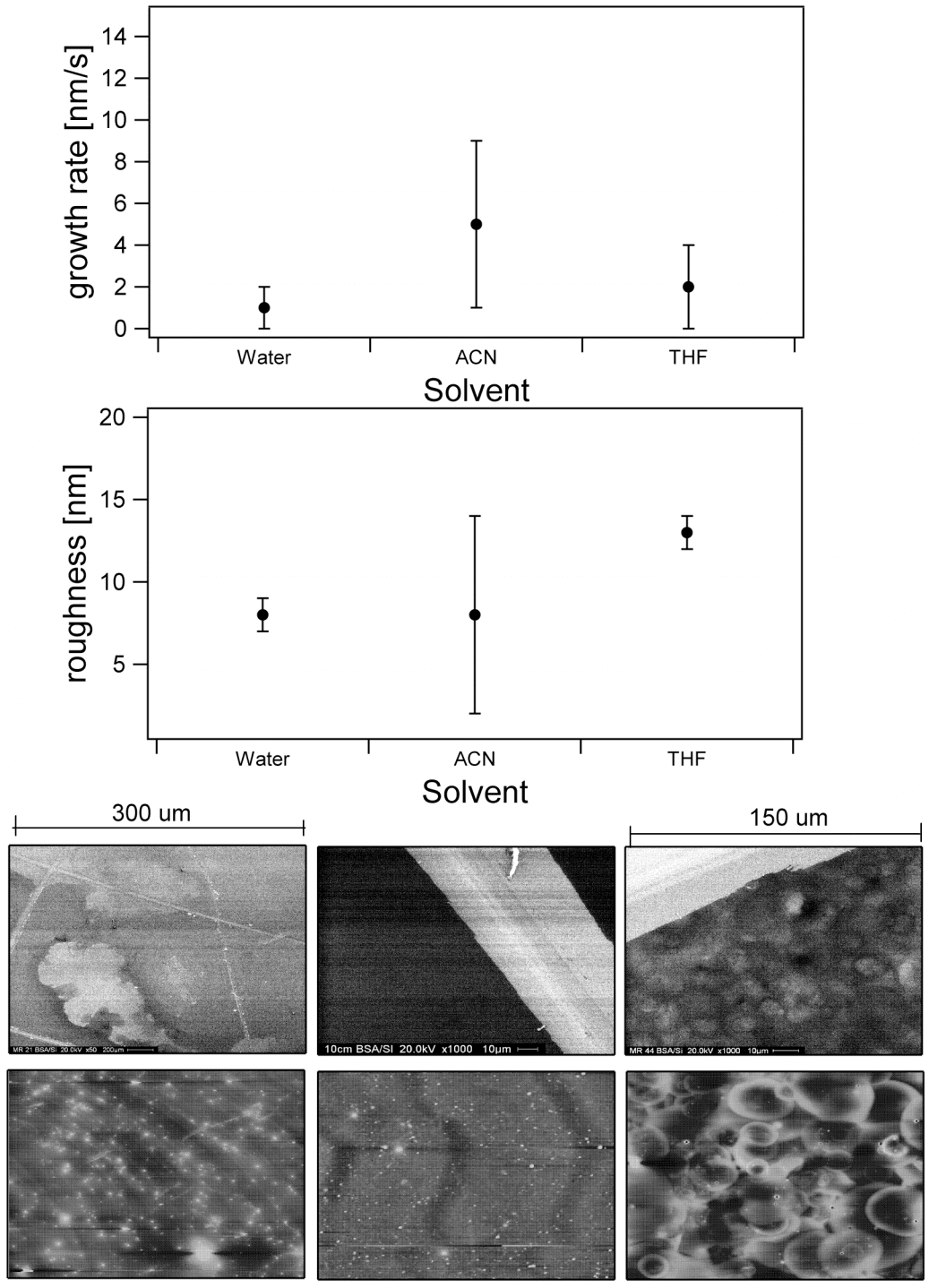


Figure illustrates the effect of vapor pressure on film roughness and growth rate in the high flux regime. The scale bars indicate 300 µm (SEM water sample) and 150 µm (ACN and THF sample). AFM (100 nm scale) is of area 80 x 80 $\mu m^2$.

Therefore, in order to create a complete film using the THF-based spray solution, the intake valve was opened in an attempt to find an appropriate solution flux sufficient enough to equilibrate the high vapor pressure of the spray solution. The airbrush parameters for this deposition were as follows: intake valve setting of 5 rotations, carrier gas pressure of 30 psi, BSA concentration of 1 mg/ml, and an airbrush to substrate distance of 10 cm. The deposition time was 12 sec. The average roughness of the film created with the THF-based spray solution is shown in figure 28 along with average roughness of the films generated with the ACN-based and water-based spray solutions and their corresponding SEM and AFM images. Note the average roughness and AFM image related to the sample created with water-based spray solution was measured on a puddle residue. The average roughness of the samples created with the water spray solution was 8 nm ± 1 nm. The average roughness of the samples generated with the ACN-based spray solution was 8 nm ± 6 nm. The average roughness of the samples related to the THF-based spray solutions were 13 nm ± 1 nm. Though some circular residues appear in the AFM image for the films generated with the THF-based spray solution, the average roughness lies within the standard deviation of the films generated with ACN-based spray solutions indicating that these films may have been generated at the lower limits (i.e. the solution flux onto the sample was slightly less than required to balance the effect of vapor pressure) of high flux mode.

In summarizing the results of chapter 2, the vapor pressure of the spray solution plays an important role in both low flux, and high flux growth regimes. Films created in low flux conditions are composed of ring like residues exhibiting little coalescence. Since

film growth in this regime is primarily driven by droplet stacking (i.e. droplets evaporate on surface completely before subsequent droplet arrive), droplet size becomes the principle factor affecting film roughness. As was observed in figure 17, increasing carrier gas pressure, which in turn reduces the droplet size, resulted in a reduction of average film roughness (figure 21). Increasing the vapor pressure also reduces droplet size, though instead of size reduction via mechanical vibrations, reduction of droplet size is achieved by increasing the vapor pressure of the spray solution which in turn serves to reduce the average film roughness.

In the high flux regime, coalescence and redissolution of residues via solvent spreading on the surface is the primary mechanism of film growth resulting in a smooth deposit. In this regime, vapor pressure must carefully be balanced with solution flux onto the sample in order to obtain smooth and complete films. If the vapor pressure of the spray solution is too low for the solution flux, incomplete films will occur as a result of solution beading and run-off from the sample. Employing a spray solution with a vapor pressure that is too high for the solution flux diminishes the ability of solvent to adequately wet the surface. Consequently, a complete film created in this manner will likely not be as thin or as smooth as a film created where amount of coalescence and redissolution of residues achieved is carefully equilibrated between the vapor pressure of the spray solution and solution flux onto the sample. Finally, a study into the effect of film growth on surface will be explored in the next chapter.

## Chapter 4

In chapter 3, the effect of the vapor pressure of spray solution in both the low flux and high flux regimes was examined. In the low flux regime (i.e. droplets evaporate on the surface before subsequent droplets arrive) increasing the vapor pressure influences the evaporation rate of droplets as they leave the nozzle and approach the sample surface. Increased atomization of droplets resulted in a reduction of film roughness, as observed in figure 17. In the high flux regime, complete and smooth films require a balance to be struck (figure 21) between the solution flux onto the sample and the vapor pressure of the spray solution. In this chapter, the effect of the surface (hydrophobic and hydrophilic) will be explored in both the high flux and lox flux regimes via AFM and SEM analysis. Hydrophobic and hydrophilic surfaces were created (hydrogen passivation and standard clean-1) as cited in chapter 1. As a comparison, the films created on the hydrophobic and hydrophilic samples were compared to films from chapter 1 that were cleaned (i.e. solvent clean) with acetone, methanol, and DI water. Samples that were solvent cleaned can be thought of as having a surface somewhere between totally hydrophobic and totally hydrophilic.

**Figure 29 - Effect of surface in low flux regime**

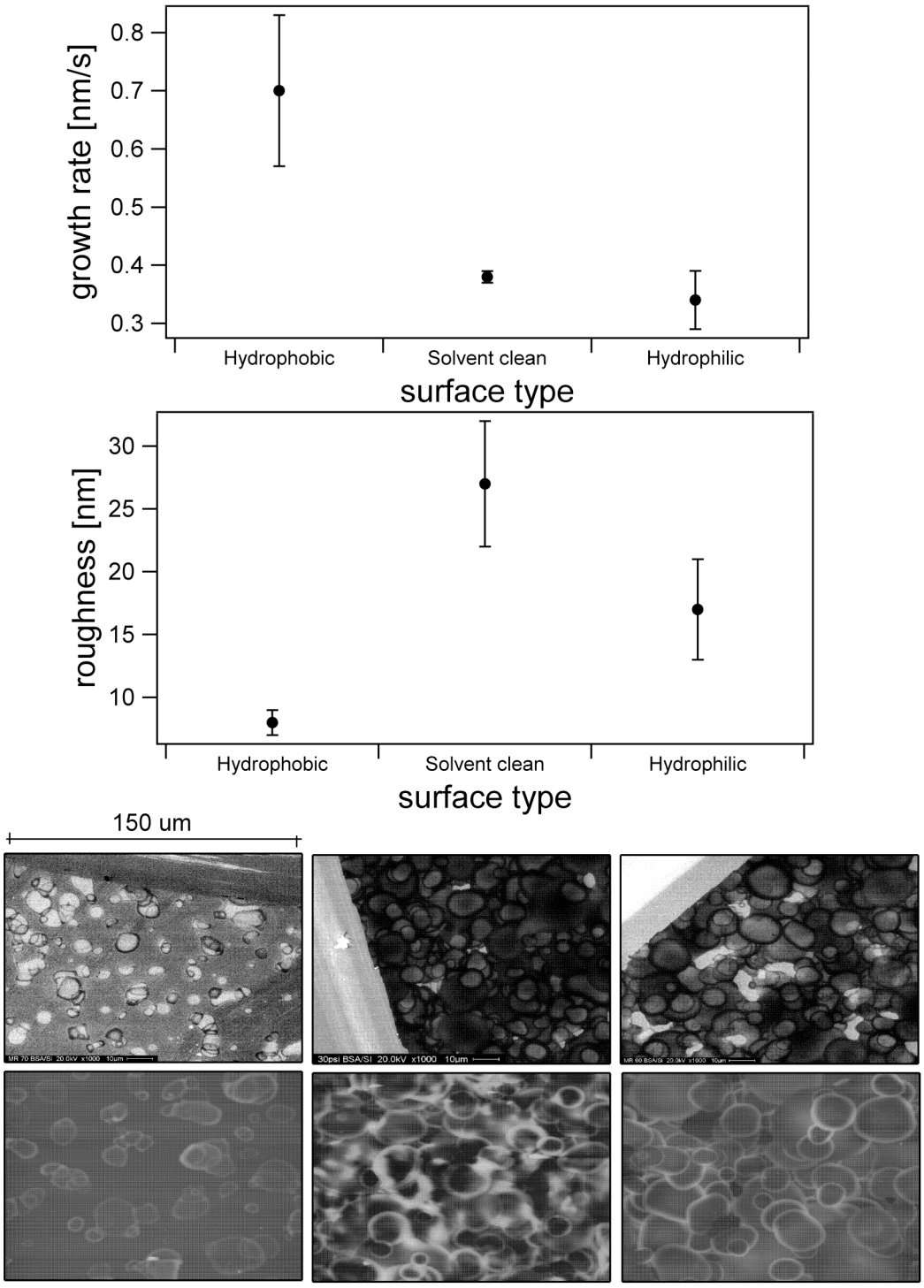


Figure illustrating the effect of surface in the low flux regime. The fixed parameters were 1.5 rtn, 30psi, 1 mg/ml, 15 cm, and 900 sec. The scale bar for the SEM images indicates 150 μm for each image. AFM (500 nm scale) is of area 80 x 80 $\mu m^2$.

**Low flux**

Figure 29 illustrates the average roughness and growth rate dependence on the substrate surface in the low flux regime. The airbrush parameters were an airbrush to substrate distance of 15 cm, a carrier gas pressure of 30 psi, an intake valve setting of 3.5 thumbwheel rotations, and a BSA concentration (4:1 ACN: water) of 1 mg/ml. The deposition time for each sample was 50 seconds. Upon examination of the AFM and SEM images related to the depositions on the hydrophobic surface, it is clear to see that a complete film was not achieved. Consequently, the roughness data point (8 nm ± 1 nm) corresponding to the films on the hydrophobic surface was determined by AFM measurement on top of a residue and the growth rate was determined by performing a step height measurement along the residue and then dividing by the deposition time As expected, a reduction in average roughness was observed between the solvent cleaned and the hydrophilic samples, 27 nm ± 5 nm and 17 nm ± 4 nm respectively. Note the AFM images have a height scale of 500 nm and the SEM images are shown at 1000x.

**Figure 30 – Effect of surface in the high flux regime**

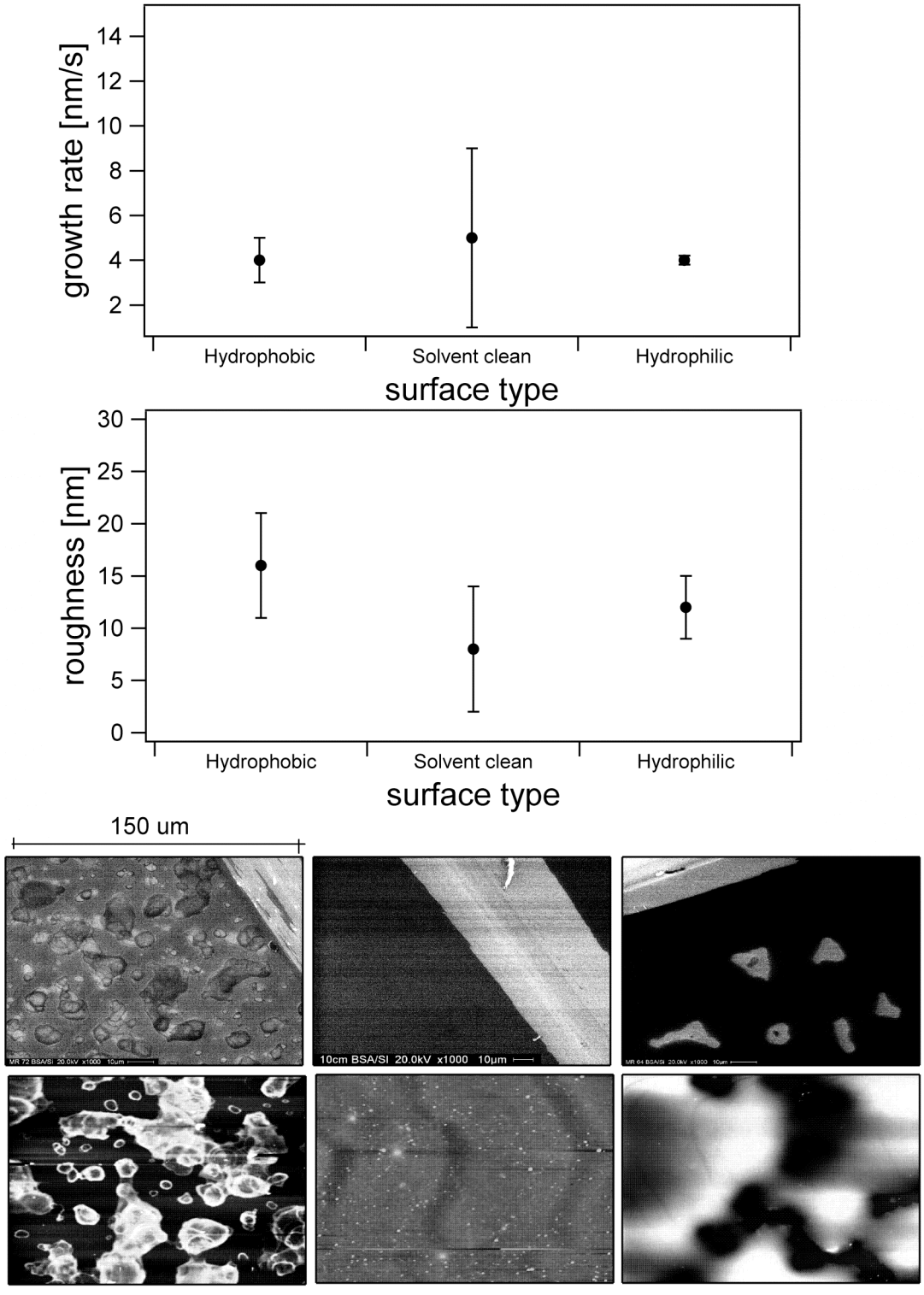


Figure illustrating the effect of surface in the high flux regime. The scale bar indicates 150 µm for each of the SEM images shown at 1000x. AFM (500 nm scale) is of area 80 x 80 $\mu m^2$. The fixed parameters were 10 cm, 3.5 rt, 30 psi, 1 mg/ml, and 10 sec deposition time.

**High flux**

Figure 30 illustrates the dependence of average film roughness and growth rate on the substrate in the high flux regime. The airbrush deposition parameters were an airbrush to substrate distance of 10 cm, a carrier gas pressure of 30 psi, an intake valve setting of 3.5 thumbwheel rotations, and a BSA concentration of 1 mg/ml (ACN: water 4 :1). The deposition time for the samples related to figure 30 was 10 seconds. Once again, a complete film was not achieved on the hydrophobic sample surface. As a consequence, AFM measurements of the hydrophobic samples were conducted on top of a residue. An average roughness of 16 nm ± 5 nm was achieved for the hydrophobic samples. An average roughness of 8 nm ± 6 nm was observed for films on which the sample was solvent cleaned, while an average roughness of 12 nm ± 3 nm was achieved on the hydrophilic samples. Though a slight increase in average roughness was observed for the films on the hydrophilic samples, as compared to those on the solvent cleaned samples, the average roughness falls within the standard deviation. Note AFM images have a height scale of 100 nm and SEM images are shown at 1000x.

In summary of the results of chapter 4, the effect of the substrate on film roughness and growth rate was investigated. Hydrophobic and hydrophilic silicon substrates were made by hydrogen passivation and oxidation (RCA standard clean-1) of the substrate, respectively. In both the low flux and high flux regimes a complete film was not achieved on a hydrophobic substrate. Droplets that impinged on the hydrophobic substrate were immediately forced off the substrate by the nitrogen gas flow during

deposition. The residues that were observed in the SEM and AFM images were likely a result of droplets that leave the airbrush just prior to termination of the deposition. These droplets are therefore are allowed to evaporate on the surface leaving behind a large residue.

A significant reduction in average roughness was observed, in figure 16, for the films on the hydrophilic substrate when compared to those on the solvent cleaned substrate. In the low flux regime, where film growth is driven by droplet stacking, improvement in the average roughness of films can be attributed to a reduction in the contact angle of droplets impinging on the surface, as evidenced by a larger residue diameter on the hydrophilic substrate versus the solvent cleaned substrate.

In the high flux regime, film growth is dominated by coalescence and redissolution of residues as solution flux onto the surface and evaporation rate of spray solution on the surface is in equilibrium. As a result, the effect of a more hydrophilic surface, and its associated improved contact angles, only weakly influence average film roughness. The next chapter will explore the fabrication of an E. coli waveguide biosensor.

# Chapter 5

As a practical extension of the results from the previous chapters, an E. coli waveguide biosensor was fabricated using the airbrush deposition technique. A sandwich immunoassay was performed to demonstrate successful deposition of the E. coli antibody. As mentioned earlier, the airbrush deposition technique is a simple, low-cost alternative deposition method which is suitable for industrial application.

## Experimental section

A sandwich immunoassay waveguide biosensor was fabricated using the airbrush deposition technique. A 0.5 mg/ml spray solution containing E. coli antibody O157: H7 (ATCC#35150) was airbrushed (airbrush parameters discussed below) onto a clean glass microscope slide. A sample of E. coli O157: H7 (ATCC#35150) was grown overnight on a TSA plate at 37 degrees Celsius and was suspended in 2PBS (0.01 M Sodium Phosphate and 0.01 M Sodium Chloride Buffer) to a desired concentration of $1.95 \times 10^7$ CFU/ml. The microscope slide was than exposed to 1.6 ml (3.12 x 107 CFU) of this sample and incubated for 30 minutes at room temperature. The slide was then rinsed three times with 2PBS and 0.05% Tween 20. AlexaFluor 647 labeled goat anti-*E. coli* O157:H7 (KPL, Gaithersburg, MD) (labeled on 4/29/08 by Sonia Magana, conc. 1.3 mg/ml, D/P=3.3) was diluted in 2PBS to make a 10 µg/ml detector antibody solution. A

volume of 0.8 ml was then incubated on slide for 15 minutes at room temperature. Slide was then rinsed 3 times with 2PBS and dried with air. Slide was imaged on HLAB-5000 (camera settings= 4 gain and 30 second exposure).

**Preparation of waveguide**

In the previous chapters it was determined that the airbrush deposition technique offers flexibility in controlling film roughness and morphology. Moreover, airbrush parameters can be adjusted to compensate for each other (e.g. opening the intake valve and reducing the distance between the airbrush and sample). Also, two types of film morphologies can be produced depending on how the airbrush parameters are adjusted. In the low flux regime, resulting films are composed of ring like residues stacked on top of each other showing little coalescence. In the high flux regime, very smooth films are created as a result surface wetting balanced by the evaporation rate of the spray solution. With these results in mind a set of deposition parameters were selected for preparing the waveguide.

In order to improve antigen capture, airbrush parameters were chosen such that the resulting film generated would exhibit a relatively large roughness and associated surface area (i.e. deposition in the low solution flux regime). The airbrush parameters were as follows: an intake valve setting of 1.5 thumbwheel rotations, a carrier gas pressure of 30 psi, an airbrush to substrate distance of 15 cm, and an antibody solution concentration of 0.25 mg/ml. The spray solution was created by dissolving the E. coli

antibody in pure DI water. Additional solvents such as ACN and THF were not used in order to prevent denaturation of the antibody. The deposition time was 900 sec.

**Antigen detection**

Detection was achieved by focusing laser (635 nm) on to the proximal end of the glass slide. As mentioned earlier, this detection method makes use of evanescent waves resulting from total internal reflection. The immobilized tagged detection antibody fluoresces, as a result of the evanescent wave, and can be detected by the CCD camera. The image, shown in figure 31, is a gray scale image showing the total fluorescence detected at each point. Bright white areas indicate large E.coli capture.

**Figure 31 - Image capture of E. coli detection**

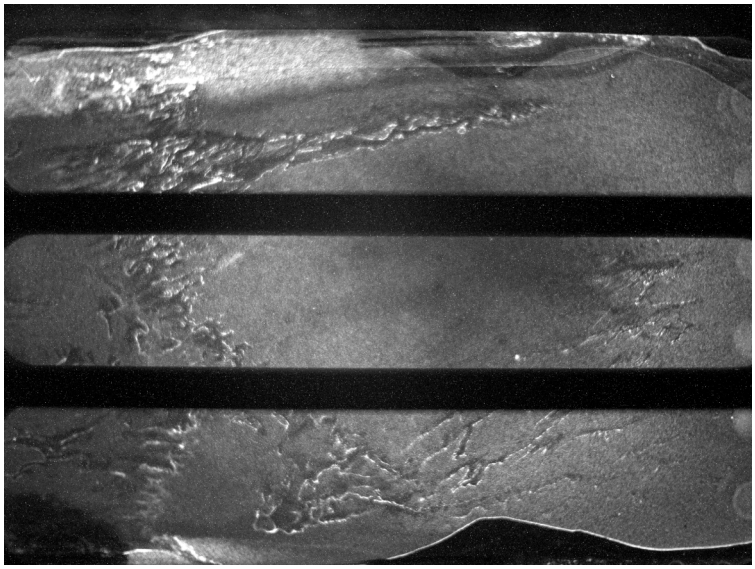

Figure shows the fluorescence intensity resulting from E .coli capture as detected by the HLAB5000.

The result of this experiment (figure 31) clearly indicates the potential for airbrush deposition in the fabrication of the E. coli waveguide biosensor; however efficacy and selectivity of a biosensor fabricated in the airbrush methodology warrants further experimental analysis. For example, exposing the waveguide biosensor to different antigens, such as salmonella or streptococcus, followed by imaging using the HLAB 5000 would speak to the selectivity of the device. The airbrush parameters of the antibody film were chosen such that the resultant film would exhibit a larger surface area and average roughness. The effect of average film roughness of device efficacy could be explored by varying the airbrush parameters during deposition along the length of the microscope slide. Finally, shelf life experiments could be conducted such that the devices ability to capture E. coli could be monitored over time.

In summary, a waveguide sandwich immunoassay biosensor was fabricated using the airbrush deposition. The airbrush parameters for the E. coli antibody film were chosen using the results of the previous experiments such that the resultant film would exhibit a rougher morphology with larger surface area. E.coli detection was performed using the HLAB5000 and demonstrated the potential (figure 22) of the airbrush deposition technique.

**Conclusion**

In conclusion, the airbrush deposition methodology offers flexibility for film deposition and is suitable for large scale industrial applications. A comprehensive study of thin film formation was investigated using BSA sprayed from a "double action" airbrush. "Double action" refers to the ability of the carrier gas pressure and solution injection into the gas stream to be controlled independently of each other.

In chapter 2, the effect of carrier gas pressure, intake valve opening, distance between the airbrush and substrate, and concentration of spray solution was investigated on spray rate, droplet size, and film roughness via SEM and AFM analysis. The results indicate the only parameter that significantly affects droplet size is carrier gas pressure. Increasing the carrier gas pressure reduces the droplet size. The parameters of intake valve opening (thumbwheel rotations) and distance between the airbrush and substrate affect the solution flux onto the surface. The concentration of spray solution did not have a significant impact on droplet size.

As a result of thin film analysis it was concluded that there are two principal growth regimes. In the low flux growth regime, droplets evaporate on the surface before subsequent droplets arrive. Thus, films grown in this regime are composed of circular residues and have a relatively large associated roughness. In the high flux regime, droplets do not evaporate before subsequent droplets arrive and thus coalescence on the sample surface is observed resulting in a very smooth deposit. In the high flux growth regime surface wetting must be carefully controlled in order to obtain smooth and complete films.

In chapter 3, the effect of the vapor pressure of the spray solution on film roughness was assessed through SEM and AFM analysis in both regimes. In the low flux regime films roughness is dependent on droplet size. Increasing the vapor pressure of the spray solution increases the evaporation rate of droplets in route to the sample resulting in smaller droplets. When operating the airbrush in the high flux regime, the vapor pressure of the spray solution and the solution flux onto the sample surface must be carefully balanced to achieve a complete smooth film. Determining the correct solution flux for creating smooth films will largely depend on the spray solution and the substrate and therefore some trial and error is required.

In chapter 4, the effect of the substrate (hydrophilic verse hydrophobic) was investigated on film roughness and compared to films on a solvent cleaned substrate. Complete films were not able to be achieved on a surface that was completely

hydrophobic. A reduction in average film roughness was achieved in the low flux regime, likely a result of a more favorable contact angle for droplets that have impinged onto the hydrophilic substrate. In the high flux regime redissolution and coalescence of residues dominate film growth; therefore an improved contact angle only has slight influence on the average film roughness.

Finally in chapter 5, a waveguide was fabricated using the airbrush deposition technique and used in a sandwich immunoassay. Using the findings of the pervious chapters the airbrush deposition parameter were chosen to create a film with suitable morphology. The results indicate capture of E.coli and thus demonstrate a practical application of the airbrush deposition technique.

## References


1. L. Li, J.S. Yu, X.Q. Tang, et al., Journal of Luminescence, 128(11), 2008: p. 1783-1786.

2. M. Schidleja, C. Melzer and H. von Seggern, Frequenz, 62(3-4), 2008: p. 100-103.

3. C. Girotto, D. Cheyns, T. Aernouts, et al., Organic Electronics, 9(5), 2008: p. 740-746.

4. T.B. Singh and N.S. Sariciftci, Annual Review of Materials Research, 36, 2006: p. 199-230.

5. Y.Y. Noh, X.Y. Cheng, H. Sirringhaus, et al., Applied Physics Letters, 91(4), 2007: p. 3.

6. Z. Xie, B.M. Henry, K.R. Kirov, et al., Thin Solid Films, 511, 2006: p. 523-528.
7. Y.H. Xiu, D.W. Hess and C.R. Wong, Journal of Colloid and Interface Science, 326(2), 2008: p. 465-470.

8. A.L. Hart, W.A. Collier and D. Janssen, Biosensors & Bioelectronics, 12(7), 1997: p. 645-654.

9. J. Magulick, M.M. Beerbom and R. Schlaf, Thin Solid Films, 516(9), 2008: p. 2396-2400.

10. C. Camilloni, A.G. Rocco, I. Eberini, et al., Biophysical Journal, 94(12), 2008: p. 4654-4661.

11. M. Cloupeau and B. Prunetfoch, Journal of Electrostatics, 22(2), 1989: p. 135-159.

12. A. Peeler, *Paint Distributer,* 1882

13. T.G. Roger Gorringe, *The Complete Airbrush Course*. 1989, New York: Van Nostrand Reinhold.

14. M.G. Westmore, Clinics in Dermatology, 19(4), 2001: p. 406-412.

15. C.J. Rogers, Aesthetic Surgery Journal, 25(4), 2005: p. 413-415.

16. Z.X.Zachary S.F.Brent J.L.Z.H.F. Corey E. Walker, *Investigation of Airbrushing for Fabricating Microelectrodes in Microfluidic Devices*. 2008. p. 663-670.

17. C. Cornila, A. Hierlemann, R. Lenggenhager, et al., Sensors and Actuators B: Chemical, **25**(1-3), 1995: p. 357-361.

18. T. Echigo, S. Naka, H. Okada, and H. Onnagawa, Jpn. J. Appl. Phys, 41, 2002: p. 6218 - 6222.

19. R. Green, A. Morfa, A.J. Ferguson, et al., Applied Physics A: Materials Science & Processing, 92(3), 2008: p. 033301.

20. I. Sayago and E. Terrado, Synthetic Metals, 148, 2005: p. 15-19.

21. I. Sayago, E. Terrado, M. Aleixandre, et al., Sensors and Actuators B-Chemical, 122(1), 2007: p. 75-80.

22. S. Lejon, J.F. Cramer and P.A. Nordberg. *Structure of Human Serum Albumin with S-Naproxen and teh GA module*. 2008 [cited 2008 Nov 9]; Available from: www.rcsb.org/pdb.

23. J. Cordova, J.D. Ryan, B.B. Boonyaratanakornkit, and D.S. Clark, Enzyme and Microbial Technology, 42(3), 2008: p. 278-283.

24. Sigma, *MSDS Bovine Serum Albumin*. 2008.

25. A.J. Yule and J.J. Dunkley, *Atomization of Melts*. 1994: Oxford University Press. UK.

26. G.G. Nasr, A.J. Yule and L. Berdig, *Industrial Sprays and Atomization: design analysis and applications*: Cromwell press, Trowbridge, Wiltshire.

27. R.D. Reitz and F.V. Bracco, Phys. Fluids, 10, 1982: p. 25.

28. R.A. Castleman, 448, 1932.

29. E.P.A. (EPA), 2008.

30. D.W. Oxtoby, W.A. Freeman and T.F. Block, *Chemisrty of Science and Change 3rd edition*. 1998: Sanders College publishing.

31. W. Kern and D. Puotinen, RCA Review, 1970.

32. G.W. Trucks, K. Raghavachari, G.S. Higashi, and Y.J. Chabal, Physical Review Letters, **65**(4), 1990: p. 504.

33. T. Tsuchiya, O. Tabata, J. Sakata, and Y. Taga, Microelectromechanical Systems, Journal of, **7**(1), 1998: p. 106-113.

34. A.M. Nardes, M. Kemerink, M.M. de Kok, et al., Organic Electronics, **9**(5), 2008: p. 727-734.

35. J.P. Kim, S.A. Lee, J.S. Bae, et al., Thin Solid Films, 516(16), 2008: p. 5223-5226.

36. R. Schlaf, H. Murata and Z.H. Kafafi, Journal of Electron Spectroscopy and Related Phenomena, 120(1-3), 2001: p. 149-154.

37. L. Reimer, *Scanning Electron microscopy*. Springer Series in Optical Sciences. 1985, Berlin: Springer-Verlag.

38. D. Instruments, *Dimension 3100 Intruction Manual*. 1997.

39. NIH. [cited; Available from: http://www.nih.gov/.

40. J. Zheng, R.E. Campbell, A.Y. Ting, and R.Y. Tsien, Nature, **3**, 2002.

41. C.f.D.C.a. Prevention. Jul, 16 2008 [cited 2008 November 9]; Available from: http://www.cdc.gov/ecoli/.

42. K. Todar. *Pathogenic E. Coli*. 2008 [cited; Available from: http://www.textbookofbacteriology.net/e.coli.html.

43. M.C. Staff. *E. coli FAQ*. 2007 [cited; Available from: www.mayoclinic.com/health/e-coli/DSO1007.

44. *Drugs and Poisons: hard science with a soft touch.* [cited 2008 Nov 9]; Available from: http://www.chem.duke.edu/~toone/labgroup/1BOSx500.jpg.

45. F.D. Fornel, *Evanescent Waves From Newtonian Optics to Atomic Optics*, ed. Springer-Verlag. 1982, Berlin Heidelberg New York.

46. T. Hirschfeld, Can. Spectroscopy, 1965.

47. F.S. Ligler, C.R. Taitt, L.C. Shriver-Lake, et al., Annual Bioanalytical Chemistry, **377**, 1992.

48. D. Toomre and D.J. Manstien, Trends in cell biology, 11(7), 2001.

49. *TIRF Theory*. [cited 2008 NOV 9]; Available from: www2.bioch.ox.ac.uk/~oubsu/ebjknigth/tritheory.html.

50. S.P. Mohanity and E. Kougianos, IEEE Potentials, 9(9): p. 44-47.

51. L. Clarck and C. Lyons, Annals of the New York Acedemey of Sciences, 1962.

52. I.E. Tothill, Computers and Electronics in Agriculture, 30(1-3), 2001: p. 205-218.

53. P. D'Orazio, Clinica Chimica Acta, 334(1-2), 2003: p. 41-69.

54. O. Bechor, D.R. Smulski, T.K. Van Dyk, et al., Journal of Biotechnology, 94(1), 2002: p. 125-132.

55. J.A. Ferguson, T.C. Boles, C.P. Adams, and D.R. Walt, Nat Biotech, 14(13), 1996: p. 1681-1684.

56. L.D. Mello and L.T. Kubota, Food Chemistry, **77**(2), 2002: p. 237-256.

57. H. Nakamura and I. Karube, Analytical and Bioanalytical Chemistry, 377(3), 2003.

58. K.A. Denton, *Rapid Detection of Mycobacterium tuberculosis in lung tissue using a fiber optic biosensor*. 2006, University of South Florida: Tampa.

59. G.P. Anderson, M.A. Jacoby, F.S. Ligler, and K.D. King, Biosensors and Bioelectronics, 12(4), 1997: p. 329-336.

60. M.J. Archer and F.S. Ligler, Sensors, **8**(6), 2008: p. 3848-3872.

61. F.S. Ligler, K.E. Sapsford, J.P. Golden, et al., Analytical Sciences, 23(1), 2007: p. 5-10.

62. C.A. Rowe-Taitt, J.P. Golden, M.J. Feldstein, et al., Biosensors and Bioelectronics, 14(10-11), 2000: p. 785-794.

63. C.A. Rowe-Taitt, J.W. Hazzard, K.E. Hoffman, et al., Biosensors and Bioelectronics, 15(11-12), 2000: p. 579-589.

64. T. Vo-Dinh and B. Cullum, Fresenius' Journal of Analytical Chemistry, 336, 2000.

65. D. Axelrod, T.P. Burghardt and N.L. Thompson, Biophysics and Bioenginering, 1984.